The Resolved Stellar Populations in NGC 1705 [1]

M. Tosi[1], E. Sabbi[2], M. Bellazzini[1], A. Aloisi[3], L. Greggio[1,4], Claus Leitherer[3], P. Montegriffo[1]

[1] *Osservatorio Astronomico di Bologna, Via Ranzani 1, I-40127 Bologna, Italy*
e-mail: bellazzini@bo.astro.it, greggio@bo.astro.it, montegriffo@bo.astro.it, tosi@bo.astro.it

[2] *Dipartimento di Astronomia, Università di Bologna, Via Ranzani 1, I-40127 Bologna, Italy*
e-mail: s_sabbi@bo.astro.it

[3] *Space Telescope Science Institute, 3700 San Martin Drive, Baltimore, MD 21218*
e-mail: aloisi@stsci.edu, leitherer@stsci.edu

[4] *Universitaets Sternwarte Muenchen, Scheinerstrasse 1, D-81679 Muenchen, Germany*
e-mail: greggio@usm.uni-muenchen.de

ABSTRACT

We present HST photometry of the resolved stellar population in the dwarf irregular galaxy NGC 1705. The galaxy has been observed with both WFPC2 and NICMOS, and successful images have been obtained in the F555W, F814W, F110W and F160W bands. The optical fields cover most of the galaxy, while the infrared field (NIC2) maps only its central regions.

The optical photometry provides ∼20000 objects down to $m_{F555W} \lesssim 29$ in the PC field of view and ∼20000 in the three WFCs. In the infrared we have been able to resolve ∼2400 stars down to m_{F110W}, $m_{F160W} \approx 26$. A subsample of 1834 stars have been unambiguously measured in all the four bands. The corresponding color-magnitude diagrams (CMDs) confirm the existence of an age gradient, showing that NGC 1705 hosts both young (a few Myr old) and very old (up to 15 Gyr old) stars, with the former strongly concentrated toward the galactic center and the latter present everywhere, but much more easily visible in the external regions.

The tip of the red giant branch (TRGB) is clearly visible both in the optical and in the infrared CMDs and allows us to derive the galaxy distance. Taking into account the uncertainties related to both the photometry and the TRGB magnitude – distance relation, we find that the distance modulus of NGC 1705 is $(m - M)_0 = 28.54 \pm 0.26$, corresponding to a distance $D = 5.1 \pm 0.6$ Mpc.

Subject headings: galaxies: evolution — galaxies: individual: NGC 1705 — galaxies: irregular — galaxies: dwarf — galaxies: stellar content

[1]Based on observations with the NASA/ESA Hubble Space Telescope, obtained at the Space Telescope Science Institute, which is operated by AURA for NASA under contract NAS5-26555

1. Introduction

Dwarf irregular and blue compact (BCD) galaxies are extremely useful to study galaxy evolution. The closest stellar systems of this type allow us to examine in detail phenomena – like the occurrence of star formation (SF) bursts and galactic winds triggered by supernova (SN) explosions, the chemical enrichment of the interstellar (ISM) and intergalactic (IGM) medium – which are important not only to understand their cosmological evolution, but also to infer the physics directly related to these processes.

Thanks to their low metallicity, late-type galaxies are fundamental to infer the primordial ^{4}He abundance (e.g. Izotov, Thuan, & Lipovetsky 1997; Peimbert, Peimbert, & Ruiz 2000), and to check the self-consistency of standard Big Bang nucleosynthesis theories. This, however, requires not only a careful analysis of the abundances derived from HII-region spectra, but also a safe understanding of the relative enrichment of the involved elements (^{4}He, ^{14}N and ^{16}O), which depends both on the SF history and on the gas flows in and out of the system. Galactic winds can be an important factor in galaxy evolution, and are suggested to be particularly effective in low-mass galaxies with strong SF activity, due to the combination of high energy input from SNe and low potential well. The detection of gaseous halos around starburst galaxies supports this idea (Heckman et al. 1993). The observed chemical properties of irregulars and BCDs, including the empirical $\frac{\Delta Y}{\Delta(O/H)}$ relation, further suggest that the galactic winds are more enriched in elements like oxygen produced by massive stars and ejected by Type II SNe (e.g. Matteucci & Tosi 1985; Pilyugin 1993; Marconi, Matteucci, & Tosi 1994; but see also Larsen, Sommer-Larsen, & Pagel 2000), than in elements like helium, mostly produced by lower-mass, longer-lived stars.

The SF history of dwarf galaxies is also crucial to check whether or not they can represent the local counterpart of the faint blue galaxies found in excess in deep imaging surveys, as suggested by e.g. Lilly et al. (1995), and Babul & Ferguson (1996). A detailed analysis of the SF history in NGC 1569 over the last 0.2 Gyr (Greggio et al. 1998, hereafter G98) has indeed confirmed that at least some of the most active dwarf galaxies have a SF rate (SFR) that would make them contributing to those counts if substained in the right time interval. What remains to be ascertained is the fraction of dwarf galaxies with a sufficiently high SFR, and the existence of such strong bursts at epochs corresponding to the redshifts where the excess is found ($z \simeq 0.7$–1.0). In this sense it becomes of primary importance to check if all the irregulars have formed stars already several Gyrs ago, and how many of them have had an intense SF activity in their remote past. As a matter of fact, the circumstance that even I Zw 18, so far considered as the prototype of really young galaxies, contains stars born at least several hundreds Myr ago (Aloisi et al. 1999, hereafter ATG; Ostlin 2000) is not sufficient *per se* to demonstrate that none of the dwarfs has started only recently ($\lesssim$ 40 Myr ago, see Izotov & Thuan 1999) to form stars.

These questions need to be quantitatively addressed in order to achieve a consistent picture on the evolution of late-type galaxies. The nearby irregular galaxy NGC 1705 is an ideal benchmark from this point of view. It is in fact one of the late-type dwarfs with the best documented proof

of an ongoing galactic outflow (Meurer et al. 1992, hereafter MFDC; Heckman et al. 2001). The outflow is likely to be strongly enriched in metals by supernova explosions and stellar winds (Sahu & Blades 1997), as often invoked by theoretical chemical evolution models of dwarf irregulars and BCDs (e.g. Marconi et al. 1994).

NGC 1705 (α_{2000} = 04 54 15.2, δ_{2000} = −53 21 40, $l = 261.08$ and $b = -38.74$) is a dwarf galaxy with apparent magnitudes $B = 12.8$ and $V = 12.3$. Its nucleus hosts a luminous super star cluster (SSC) with estimated mass $\sim 10^5$ M$_\odot$, probably a proto-globular cluster only 10 Myr old (Melnick et al. 1985; O'Connell et al. 1994; Ho & Filippenko 1996). The galaxy has been classified by MFDC as a BCD with a fairly continuous SF regime and an approximate oxygen abundance 12+log(O/H)$\simeq$8.46, similar to that of the Large Magellanic Cloud. A more precise oxygen abundance of 8.36 has been derived by Storchi-Bergmann, Calzetti & Kinney (1994) from UV, optical and near infrared spectra. Ground-based work (e.g. Quillen et al. 1995) revealed the presence of a composite stellar population, with the older ($\sim$1–10 Gyr) field population defining the galaxy morphology. UV spectra acquired with HST (Heckman & Leitherer 1997) showed that nearly half of the optical/ultraviolet light is contributed by the young stellar population, and possibly by the central SSC which may also power the observed bipolar outflow. From the lack of spectral stellar wind features, Heckman & Leitherer suggested that the stars in the most luminous SSC of NGC 1705 are not more massive than 10–30 $M_\odot$.

The distance to NGC 1705 is still relatively uncertain, and has been derived from CMDs based on pre-Costar HST images (5 ± 2 Mpc according to O'Connell et al. 1995), or from the heliocentric velocity of 628 km s^{-1} (4.7 Mpc according to MFDC, 6.2 Mpc according to Meurer et al. 1998). As shown by Sternberg (1998), at the quoted distances the SSC is overluminous for its mass and may imply an Initial Mass Function (IMF) unusually skewed in favor of massive stars.

To study in further detail the stellar populations of NGC 1705 and to infer its SF history, we have observed the galaxy with the HST cameras WFPC2 and NIC2 in the F555W, F814W, F110W and F160W filters, deriving the CMDs of its resolved stars from these datasets. In this paper we present these new data and the resulting CMDs (Sections 2, 3 and 4). From the magnitude of the TRGB (Section 5) we derive a new estimate of the distance modulus, while the comparison of the empirical CMDs with theoretical stellar evolution tracks (Section 6) indicates the major evolutionary features of the stellar populations in NGC 1705. The results are discussed and summarized in Section 7.

2. Observations and data reduction

The infrared observations were performed on 1998 March 17, and repeated on 1998 September 19 due to a suspend mode event of NICMOS for a high-energy particle hit during the first observing run. We used the F110W and F160W broad band filters and the NIC2 camera centered on the brightest SSC, which is near the center of NGC 1705.

The optical observations were performed on 1999 March 4–7 with the PC camera centered on the SSC and including the NIC2 field. A failure in the fine lock guiding mode, coupled with a failure in the star guide reacquisition, prevented us from obtaining some of the requested images in the four F380W, F439W, F555W, and F814W filters. Only the long exposures in F555W and F814W were successfully acquired. The requested long observations at shorter wavelength, as well as the short exposures in all the four filters, were rescheduled and reacquired on 2000 November 10–11. The photometric reduction of the bluer filters will be presented in a forthcoming paper (Monelli et al. in preparation).

2.1. The optical data

The data successfully acquired with WFPC2 in the first observing run correspond to eight 1300 s exposures in each F555W and F814W filters. The pointing was organized to follow a box dither pattern with CR-split 0.5. This translates into 4 different pointing positions with a point spacing of $0\farcs559$ for WFPC2, and the following offsets in arcsec: (0,0) for Point 1, (0.5,0.25) for Point 2, (0.75,0.75) for Point 3, and (0.25,0.5) for Point 4. Two exposures at each dither position were also requested for an easier cosmic-ray removal. The dithering technique is applied to improve the background estimate, identify hot pixels and smooth local pixel to pixel variations from images taken at different dither points, and improve the image sampling. A problem in the execution of the dither pattern due to a bug in the TRANS software for the translation from the Phase 2 commands to the telescope operations, resulted in 5 exposures at Point 1, and one exposure at each of the other Points. Despite this ground-based software failure, the resulting dither pattern allowed us to correctly remove cosmic rays and better sample the PSF, not affecting at all our scientific goal of measuring stellar magnitudes with a photometric error $\leq$0.2 mag down to the expected limit of $\sim$28 for both m_{F555W} and m_{F814W}.

For each filter the 8 dithered frames, calibrated through the standard STScI pipeline procedure, were combined in a single, fully sampled 10400 s image, using the software package *Drizzle* (Fruchter & Hook 1998). The effective pixel size in the resampled images corresponds to $0\farcs023$ and $0\farcs05$ for the PC and WFCs respectively. The PSF in the resulting *drizzled* images has a FWHM of 4.2, 3.3, 3.3, and 3.3 pixels in F555W for PC, WFC2, WFC3, and WFC4 respectively. The corresponding quantities in F814W are instead 4.4, 3.3, 3.2, and 3.2.

Fig. 1 shows a mosaic of the WFPC2 images in the F814W filter, obtained with the VmIm-Regrid task from the ESO VIMOS Data Reduction Software. The images were regridded to the equatorial coordinate system via a gnomonic projection given by the WCS information in the image headers. This coordinate system has an uncertainty of possibly more than $3\farcs5$, as indicated by the comparison of the WCS values taken from images at different wavelengths. The image shows that most of the galaxy falls well within the observed fields. The bright spot at the center of the PC field is the SSC, whereas the isophotal contour levels divide the galaxy in regions of different surface brightness, corresponding to different crowding conditions. Different regions are numbered from 0

(the outermost one) to 7 (the innermost region, encircled by the white contour). The indicated isophotal contours have average flux density in F814W of 2, 4, 8, 16, 32, 128, 256 counts/px, respectively. Throughout this paper we will refer to these zones as Region 0 ... 7. It is interesting to note that the isophotal contours are fairly elliptical, smooth (when not disturbed by especially bright objects) and concentric. The only exception is Region 7, which is both off-centered and distorted. The distortion is due to a sort of spiral pearl necklace (better visible in Fig. 2) apparently originating from the SSC and leading north. The SSC is not seated at the center of the isophotal contours, a circumstance confirming the suggestion by Heckman & Leitherer (1997) and Hensler et al. (1998) that the SSC is not at the galaxy center.

The photometric reduction of the images has been performed with the DAOPHOT package in the IRAF[2] environment. We have followed the same procedure described in ATG, the only difference in this case being that we have detected the stars independently in the two bands, without forcing in the shallowest frame the finding process of the objects detected in the deepest one. For each detector the objects found in both bands were cross-identified with DAOMATCH and DAOMASTER. Only the objects with a coordinate offset less than a matching radius of 2.0 pixels (corresponding approximately to half of the FWHM of the PSFs) were eventually retained. After this match we remained with 19838 objects having a measured magnitude in both F555W and F814W filters in the PC field. The corresponding numbers are 8525 for the WF2, 5711 for the WF3, and 5593 for the WF4.

The instrumental magnitude of each object in each filter and detector was estimated via a *PSF-fitting technique*. A PSF template was constructed by considering the most isolated and clean stars, sparsely distributed over each frame: 4 stars were considered for the PC, 5 for the WF2, 4 for the WF3, and 6 for the WF4. The zero point of the PSF photometry was determined with the standard *aperture photometry technique* within a 2 pixel radius aperture. The conversion of the instrumental magnitudes $m_{\rm i}$ (with the exposure time already taken into account) to the HST VEGAMAG system was performed by following the prescriptions in Holtzman et al. (1995a,b), with the updated values provided by the STScI web page (see also Biretta et al. 2000):

$$m = m_{\rm i} + C_{\rm ap} + C_{\infty} + ZP_{\rm V} + C_{CTE}.$$

$C_{\rm ap}$ is the classical aperture correction to convert the photometry from a 2 pixel to a conventional $0''.5$ radius aperture for the WFPC2 (22 and 10 pixels for PC and WFs, respectively, in our *drizzled* images). It has been directly calculated by considering the encircled energy of single stars in our observational frames. The second aperture correction C_{∞} is an offset of –0.10 (irrespective of filter and detector) to convert the magnitude from the $0''.5$ radius into a nominal infinite aperture. The zero points $ZP_{\rm V}$ are taken from Baggett et al. (1997). We have also considered the *charge transfer efficiency* (CTE) correction C_{CTE} in its new formulation by Whitmore, Heyer, & Casertano (1999).

[2]IRAF is distributed by the National Optical Astronomy Observatories, which are operated by AURA, Inc., under cooperative agreement with the National Science Foundation.

Other secondary calibrations have been neglected. The *contamination* correction with the new rates derived from Baggett & Gonzaga (1998) is practically zero for all the detectors in the two F555W and F814W filters. We have instead not applied any correction for the *short vs long anomaly* (see e.g. Casertano & Mutchler 1998), because its value has recently turned out to be more uncertain than previously thought (Casertano, 2000 private communication).

For a safe interpretation of the characteristics of the galaxy stellar populations, we need to distinguish as much as possible *bona fide* single stars from extended, blended or spurious objects. We have thus applied to our catalogs selection criteria based on the shape of the objects. To this aim we have considered the Daophot parameters χ^2 and *sharpness*: χ^2 gives the ratio of the observed pixel-to-pixel scatter in the fit residuals to the expected scatter calculated from a predictive model based on the measured detector features, while *sharpness* sets the intrinsic angular size of the objects. We have selected only the objects with $\chi^2 \leq 4$ in both filters for the PC, $\chi^2 \leq 2.2$ in F555W and $\chi^2 \leq 2.5$ in F814W for the three WFs. Moreover only detections with $-0.5 \leq$ *sharpness* ≤ 0.5 in all filters and for all detectors have been eventually retained. These χ^2 and *sharpness* values turned out to be those allowing to best reject spurious and extended objects, without eliminating also the bright stars. By inspecting the rejected objects, we have recognized several candidate star clusters (i.e. fairly round but extended objects) and background galaxies. We have 17 star clusters (besides the brightest SSC) in the PC, 4 in the WF2, 5 in the WF3 and 3 in the WF4. The candidate background galaxies are 13 in the WF2, 11 in the WF3, and 18 in the WF4. In the latter case, the 18 galaxies occupy only a restricted zone of the WF4 and the concentration is much higher than in the other fields: we are presumably dealing with a real, yet unclassified, galaxy cluster, since the derived galaxy density (18 arcmin^{-2} down to m_{F814W}=22) is almost a factor of 5 higher than that predicted by deep counts of field galaxies (e.g. Pozzetti et al. 1998).

A further selection often applied is based on the photometric error σ_{DAO}. The distribution of σ_{DAO} in the F555W and F814W bands is shown in Fig. 3 for both the PC and the three WFs. If we apply the σ_{DAO} selection criterion to the stars which have already been constrained in the χ^2 and *sharpness* parameters, with $\sigma_{DAO} \leq 0.2$ in both filters we retain 15299 stars in the PC, and 6785, 2812 and 4279 in the WF2, WF3 and WF4, respectively. Going down to $\sigma_{DAO} \leq 0.1$ implies 9224 stars retained in the PC, and 4691, 1551 and 2376 in the WF2, WF3 and WF4, respectively.

We have put all the measured stars on the common reference frame shown in the mosaic image of Fig. 1, and we have divided them into six groups according to their position with respect to the isophotal contour levels. Regions 1 and 2, and Regions 4 and 5, are considered together because both their stellar populations and their crowding conditions turned out to be very similar to each other. Region 7, despite the low number of stars, has been considered separately from the others, because it contains the brightest SSC and crowding dramatically affects its photometric accuracy and completeness, as will be shown from the artificial stars experiments (see Section 4).

2.2. The infrared data

For each filter we have acquired ten 512 s exposures with a spiral dither pattern of $0\farcs2$ for a total integration time of about 85 min. The dither technique was chosen to account for pixel-to-pixel non-uniformities, and to better sample the PSF, which is a very important component in the treatment of crowded stellar fields such as that of NGC 1705. The MULTIACCUM readout mode was adopted for each exposure in order to get rid of saturated pixels and cosmic ray events. To this purpose we considered the pre–defined sequence STEP256, which consists of 13 non-destructive array reads of 0.0 s (the bias level), 0.3 s, 0.4 s, 1 s, 2 s, 4 s, 8 s, 16 s, 32 s, 64 s, 128 s, 256 s and 512 s. The resulting combined F110W image is shown in Fig. 2 together with an enlargement of a PC portion taken from Fig. 1. The white contours delineate Regions 6 and 7 as defined in the previous sub-section.

The data reduction has been performed following the procedure described by Aloisi et al. (2001, hereafter Al01) for the twin set of NIC2 data acquired for the galaxy NGC 1569, for the same HST proposal (GO 7881) and with the same technique. The automatic CALNICA pipeline in the IRAF STSDAS package was applied to remove the instrumental signatures and co-add datasets from multiple iterations of the same exposure. Particular attention was paid to the necessary corrections for all the instrumental anomalies, artifacts and instabilities which are not automatically taken into account by the standard pipeline. Among these are the *shading*, the *pedestal*, the *cosmic ray persistence*, and the *linearity*, all effects that we have already considered in Al01. Other anomalies (see Dickinson 1999 for details on all the possible anomalies) were found in the data reduction of NGC 1705 NICMOS images. *Grot* and the *photometrically challenged column* are bad imaging regions, that we had to mask in our data. *Bands* and *bars* are image defects directly related to bias problems. Our data were affected by both of them: the use of NIC1 in parallel mode originated bands, while the circumstance that we didn't use NIC3 at all induced bars in the NIC2 images. We were able to effectively remove both bands and bars by using the most updated NICMOS-related software available in April 2000. Last but not least, our images were also affected by *electronic ghosts*, also known as *Mr Staypuft anomaly*, false faint images due to the effects of overexposures (related in our case to the brightest SSC of NGC 1705). We got rid of this image anomaly by using an algorithm kindly made available by Luis E. Bergeron of the STScI NICMOS team.

For each filter the dithered CALNICA calibrated exposures were combined into a single frame with the same *Drizzle* package used for the optical data (see previous subsection). The resulting *drizzled* image, with a pixel size of $0\farcs0375$, has a FWHM of 3.0 pixels in F110W and 3.9 pixels in F160W, instead of the original 1.4 and 1.8 pixels in F110W and F160W, respectively, of the no-resampled single frames.

The photometric analysis was performed with the IRAF package DAOPHOT. 4142 objects in the F110W frame, and 3321 in the F160W frame, were independently detected by the routine DAOFIND at 1.5 σ above the local background. The instrumental magnitude of each object was estimated via PSF fitting with a zero point calculated within a 2 pixel radius aperture. We adopted

as PSF templates the 4 stars of the field which turned out to be more isolated and unaffected by profile distortions.

The instrumental magnitudes from the PSF-fitting technique were calibrated in the HST VEGAMAG system with the formula given by Dickinson (1999):

$$m = m_{\rm i} + C_{\rm ap} + C_\infty + ZP_{\rm V}$$

where $C_{\rm ap}$ is the aperture correction to convert the magnitudes within a 2 pixel radius in the *drizzled* images into the magnitudes within the conventional $0\farcs5$ radius (in our *drizzled* case it corresponds to 13.33 pixels and not to the standard 7.6 pixels), $C_\infty = -0.152$ mag is the quantity given by Dickinson to convert the magnitude at $0\farcs5$ into the nominal infinite aperture, and $ZP_{\rm V}$ is the published zero point for the HST VEGAMAG system (22.381 for F110W and 21.750 for F160W).

The objects found in both bands were cross-identified with the routines DAOMATCH and DAOMASTER, retaining only those identifications with a difference in their coordinates within a radius of 2.0 pixels (roughly half of the PSF FWHM in F160W). In this way we selected 2373 objects having a measured magnitude in both F110W and F160W.

As for the WFPC2 objects, to distinguish as much as possible *bona fide* single stars from extended, blended or spurious objects, we have applied to our catalog the χ^2 and *sharpness* criteria. After a visual screening of each individual object which could or could not be removed depending on the adopted limits for acceptable *sharpness* and χ^2, we have retained all the objects with $-0.3 \leq$ *sharpness* ≤ 0.3. In this case a restriction in χ^2 would have inevitably removed also bright *bona fide* single stars. Of these selected objects, 1707 stars have $\sigma_{DAO} \leq 0.2$ in both filters (see Fig. 3) and 829 stars have $\sigma_{DAO} \leq 0.1$.

By inspecting the rejected objects, we have recognized all the candidate star clusters found in the portion of the PC image falling in the NIC2 field. They are marked in Fig. 2 as open circles. If we assume that the galactic barycenter is most likely located near the center of Region 6 and of all the other isophotal contours, except Region 7, it is interesting to note that the candidate clusters are not evenly distributed around the center and seem to avoid the area close to the SSC. We consider this as a real segregation since we have not found any reason to ascribe it to selection effects in the candidate cluster identification. The properties of the candidate clusters will be discussed in a forthcoming paper (Monelli et al. in preparation) when the F380W and F439W images will also be examined and the colors will be measured.

As already done for the optical data, the stars have been divided into groups, using the same isophotal contours of the WFPC2 F814W mosaic image. Due to the smaller size of NIC2, these groups contain stars only from Regions 4-5, 6 and 7. Region 7 includes the most luminous SSC and most of the brightest stars.

We have also cross-identified the stars appearing in both the PC and NIC2 field of view by considering a matching radius of 2 pixels (about half of the PSF FWHM in all the four filters). Our final sample includes 1834 stars and 11 candidate clusters with measured magnitudes in all

the four F555W, F814W, F110W and F160W frames.

3. Color-magnitude diagrams

Fig. 4 shows the m_{F814W} *vs* $m_{F555W} - m_{F814W}$ CMDs of all the stars measured in the seven Regions described in the previous section. The number of objects in each panel is labelled in its lower right corner. As mentioned above, Regions 1 and 2 are plotted together because both their populations and their crowding conditions are very similar. The same occurs for Regions 3 and 4. The spatial distributions of the stellar populations in the various Regions are clearly different from one another. Bright stars are mostly concentrated toward the galactic center and only a few of them are present in the outer regions. Instead, faint stars are probably everywhere but are more easily resolvable in the external regions, thanks to the less crowded conditions.

The two innermost Regions present a well defined blue and red plume. The blue plume is located at $m_{F555W} - m_{F814W} \simeq -0.1$, with the brightest stars at m_{F814W}=20.3, and corresponds to the main-sequence (MS) evolutionary phase and to the hot edge of the core helium burning phase. The red plume is at $m_{F555W} - m_{F814W} \simeq 1.7$ and extends up to m_{F814W}=19.5. It is populated by red supergiants (RSGs) at the brighter magnitudes and asymptotic giant branch (AGB) stars at fainter luminosities. The brightest stars, of whatever color, are all located in Region 7, and correspond to the pearl necklace visible in Fig. 2 and described in the previous Section. The severe crowding of Region 7 prevents a reliable detection of objects fainter that about 25.5 in either the F555W or the F814W band. Region 6 is sufficiently less crowded to allow for the detection of much fainter objects, and already shows the concentration of stars with $1 \leq m_{F555W} - m_{F814W} \leq 1.8$ and $24.2 \leq m_{F814W} \leq 26$, which is much better delineated from Region 5 outwards and corresponds to low–mass, old, stars in the red giant branch (RGB) evolutionary phase. Regions from 3 to 0 contain very few, if any, stars outside the RGB.

Fig. 5 shows in the upper panels the infrared CMDs of the galaxy field covered by NIC2 (Regions 4–5, 6 and 7). In this case, only a few stars are found in the bluest part of the diagram. This is not due to a real lack of young stars (as we know from their conspicuous presence in the optical CMD), but to the intrinsic faintness of hot stars in the infrared bands. The red plume at $m_{F110W} - m_{F160W} = 1$ is instead very well sampled and shows a tight vertical finger with m_{F160W} from 18 to 20 plus a clump of fainter stars with $0.6 \leq m_{F110W} - m_{F160W} \leq 1.6$. Once again, the brightest stars are concentrated in Regions 6 and 7, with the bluer objects visible only in the latter one.

The three lower panels of Fig. 5 show the CMDs with the largest color baseline for the objects common to all the four bands: the different evolutionary phases are better separated, but the overall distribution does not change. The CMD in other bands of the same objects can be seen in Annibali et al. (2001). In order to check the fraction of spatially coinciding objects in the four filters with physically meaningful colors and therefore correctly cross-identified, we have inspected the position of the 1834 stars in all the possible combinations of CMDs in the four bands. We find

that the objects keep consistently their colors in the various band combinations (e.g. blue and red objects in $m_{F555W} - m_{F814W}$ remain blue and red, respectively, also in the other colors). This circumstance indicates that we are dealing with intrinsic, physical features of real stars and not with spurious colors due to chance spatial coincidence of different objects. Having already removed from this sample the objects turned out to be candidate clusters or galaxies on the basis of the shape selection criteria, we can consider these 1834 objects as the safest sub-sample of *bona fide* single stars in the central region of NGC 1705.

Notice that this positive result is not always achievable in such crowded fields, both because of the high probability of finding multiple objects spatially overlapping and because of the very different fluxes of cool and hot stars in different photometric bands. As discussed in detail by Al01, the probability of success depends on the combination of crowding, wavelength separation of the available bands, and SF history of the examined region. For instance, in the case of NGC 1569, for which we had no F814W image available, we have been able to unambiguously cross-identify only a few stars present in the F110W and F160W frames (analyzed by Al01) and in the F439W and F555W frames (analyzed by G98). This is because NGC 1569 is very crowded, and has experienced a strong SF burst in the last 0.1 Gyr and a conspicuous SF activity between 1.5 and 0.15 Gyr ago. The recent burst provides a large number of hot stars, bright in blue filters but faint in red ones, while the previous SF episode provides a large number of cool stars, bright in red filters but faint in blue ones. These two populations are spatially coincident and it is thus inevitable that the flux peaks detected in different passbands actually correspond to different stars. The wavelength selection effect is also what causes the blue plume of the optical CMD to be poorly defined in the near-infrared (NIR) diagram of Fig. 5 and, conversely, the vertical red finger of the NIR CMD to be sparser in the optical one. This effect has been found and discussed also in other galaxies (see, e.g., Schulte-Ladbeck et al. 1999b for VII Zw 403). The artificial stars experiments described in the next section give a more quantitative description of these wavelength selection effects.

4. Role of incompleteness and blending

The photometry at the faint magnitudes reached by our data and in such crowding conditions is certainly affected by incompleteness and blending. In order to quantify these factors as a function of magnitude, we have performed a series of artificial stars experiments, following the procedure briefly described here.

4.1. Artificial stars experiments

Artificial star experiments have to probe the observational effects associated with the whole process of data reduction of a given frame, i.e., for instance, the accuracy of the photometric measures, the crowding conditions, the ability of the PSF-fitting code in estimating the sky level or

in resolving partially overlapped sources, etc. It is of the utmost importance that the artificial stars do not interfere with each other since in that case the output of the experiments would be biased by *artificial* crowding, not present in the original frame. To avoid this potentially serious bias we have divided the frames in grids of cells of known width, and we have randomly positioned *only one artificial star per cell* at each run (a similar procedure has recently been adopted by Piotto & Zoccali 1999). The additional constraint is that each star must have a distance from the cell edges sufficiently large to guarantee that all its flux and background measuring regions fall within the cell. In this way we can control the minimum distance between adjacent stars. At each run the absolute position of the grid is randomly changed in a way that, after a large number of experiments, the stars are uniformly distributed in coordinates.

The stars were distributed in magnitude with a function similar to the observed luminosity function (LF), except for an excess of faint stars below the detection limit of our observations. This was to probe with sufficient statistics the (faint) range of magnitudes where the incompleteness is expected to be most severe. We have simulated about 10^5 stars for each WFPC2 camera and filter, and about 2×10^5 for each NIC2 image. The whole series of performed experiments provides 1.2×10^6 artificial stars, for which we have memorized input and output magnitudes, and any other useful parameter. Stars with input–output magnitude $\Delta m > 0.75$ were considered *lost* because such a difference implies that they fell on a real star of their same luminosity or brighter.

The artificial stars have been projected onto the same reference frame of Fig. 1 and separated in the corresponding radial regions (six annuli for the F555W and F814W filters, and three for the F110W and F160W filters) to allow the characterization of incompleteness and blending in the different regions of the images. The frames have been re-reduced following exactly the same procedure as for the real stars, and the same selection criteria for χ^2 and *sharpness* (see Sections 2.1 and 2.2) have been applied.

Fig. 6 and Fig. 7 show the input–output magnitude of the artificial stars resulting from our tests. Δm_{F555W} and Δm_{F814W} are plotted as a function of m_{F555W} and m_{F814W}, respectively, for each Region from 0 to 7. Fig. 8 shows instead Δm_{F110W} and Δm_{F160W} as a function of the input m_{F110W} and m_{F160W} for the three inner Regions. The solid lines superimposed to the plotted distributions report the mean Δm (central lines) and the $\pm 1\sigma_m$ around the mean. The value of σ_m at three reference magnitude levels are also reported in each panel to provide an easier and quantitative comparison.

Each of the figures presented above provide a complete and statistically robust characterization of the photometric errors and of the effects of blending affecting our observations. In what follows we will refer to Fig. 6 as an exemple to describe the general trends that are present in all these plots.

- The σ_m provide the best estimate of the random component of the actual photometric error affecting our data. By comparing them with the σ_{DAO} plotted in Fig. 3, it is apparent that the latter increasingly underestimate the actual errors towards fainter magnitudes.

- The mean Δm provides a full description of the systematic component of the photometric error, due to the average effect of blending as a function of magnitude. In all panels the mean Δm begins to deviate from zero around $m_{F555W} \sim 26$, becoming increasingly large toward faint magnitudes. This means that many stars are recovered with a brighter magnitude than their input one, because they are blended with a fainter star that is present in the original frame. Approaching the limiting magnitude of the observations (at $m_{F555W} > 28$) artificial stars are recovered *only* if they are pushed up above the detection threshold by blending with an undetected real star and/or a positive fluctuation of the background noise.

We will make full use of the extensive set of artificial star experiments for the production of proper synthetic CMDs that will allow the reconstruction of the star formation history of the galaxy. This part of the analysis will be described in a companion paper (Annibali et al. in preparation). In the following, we shortly comment on the effects of blending and incompleteness to assess the overall accuracy of our photometry, with particular attention to the impact on the distance estimate discussed in Section 5.

4.2. Blending and completeness

From the inspection of Fig. 6, Fig. 7 and Fig. 8 it is clear that the very concentrated population of bright stars in Region 7 produces a high degree of incompleteness at faint magnitudes in this region. The high degree of crowding and the high level of sky background produced by the wings of the many bright stars results in much larger photometric errors and brighter limiting magnitude than in all the other Regions (0-6). Outside of this very central part, the behavior of Δm as a function of magnitude is quite similar and very well sampled everywhere.

It is particularly interesting to check at which magnitude the effects of blending become significant, i.e. at what level Δm significantly deviates from zero. First of all we note that the mean value of Δm is always lower than σ_m, thus random errors dominate over the systematics associated with the blending at every magnitude. Second, in the Regions from 0 to 6, the mean Δm is lower than 0.05 mag for $m_{F555W} < 24$, $m_{F814W} < 23$, $m_{F110W} < 22.5$ and $m_{F160W} < 21.5$ respectively. Therefore the effect of blending can be considered negligible down to very faint magnitudes. The above limits become significantly fainter if the most external regions are considered (0-2). In Region 0, which covers a large fraction of all the WF cameras, the average Δm is still virtually null at $m_{F555W} = 26$ and $m_{F814W} = 25$ (see also Fig. 9, below).

The *completeness factor* $CF(m) = N_{out}/N_{in}$ (where N_{in} is the number of artificial stars added and N_{out} is the number of artificial stars successfully recovered for a given magnitude bin in a given passband m) is a measure of the probability of detection of a real star at a given magnitude, as long as blending is negligible. When blending is not negligible a correct evaluation of $CF(m)$ should take it into account. In a CMD, the global completeness factor is given by the product of the factors in the two involved passbands, hence it is also a function of the color index. In Fig. 9 four curves

representing levels of equal $CF(m_{F814W}, m_{F555W} - m_{F814W})$ are superimposed to the CMDs of the different regions in which we have divided our sample. From top to bottom they correspond to $CF = 0.95$ (thick line), $CF = 0.75$ (thin line), $CF = 0.50$ (thick line), and $CF = 0.25$ (thin line). Note that in the outer Regions (0-5) the $CF = 0.50$ level occurs at $m_{F814W} > 24$ for any given color in the observed range. In particular, the TRGB (at $m_{F814W} \sim 24.5$ and $m_{F555W} - m_{F814W} \sim 1.6$) lies ~ 1.5 mag above this level.

An evenly spaced grid of blending vectors is also superimposed to the CMDs (thin lines with black dots) in Fig. 9. The amplitude of these vectors is the average Δm described above, the dots indicate the direction of the vectors. The effect of such vectors become appreciable only for $m_{F814W} \geq 24$ in Regions 5 and 6, and $m_{F814W} \geq 26$ for Regions 0-4 and only at extreme colors.

The analogous plot for the infrared and infrared/optical CMDs is presented in Fig. 10. In the outer Regions (4-6) the $CF = 0.50$ level occurs at $m_{F160W} \sim 22 - 22.5$ in both the CMDs and the effect of blending becomes significant over the whole observed color range only for $m_{F160W} \geq 23.5$.

5. A new estimate of the distance

While the use of the TRGB luminosity as a standard candle dates back to 1930 (see Madore & Freedman 1998, and references therein), the development of the method as a safe and viable technique is relatively recent (Lee, Freedman, & Madore 1993). In the last few years it has become a widely adopted technique (see, for instance, Ferrarese et al. 2000), with all the possible biases well characterized and quantified (Madore & Freedman 1995, hereafter MF95). The key observable is the magnitude of the LF sharp cut-off in the Cousins I passband, usually identified by applying an edge-detection algorithm to the LF of the upper RGB (see Sakai, Madore, & Freedman 1996, hereafter SMF96, for a standard application).

As apparent from the CMDs shown in the previous sections, our data allow for a good sampling of the RGB. In particular, the WF cameras sample exclusively the outer halo of the galaxy, a relatively uncrowded region dominated by low-mass RGB stars and negligibly contaminated by other sources. Thus there are favorable conditions to reliably measure I_{TRGB} and obtain a distance estimate for NGC 1705 significantly more accurate than the existing ones (O'Connell et al. 1995; MFDC; Meurer et al. 1998).

Our WF sample excellently fulfills all the requirements for a safe TRGB detection identified by MF95 by means of numerical simulations. In particular (1) the number of stars in the upper one mag bin from the TRGB is much larger than the minimum indicated by MF95 (100 stars) in any of the WF CMDs, (2) the contamination from non-RGB stars is negligible, since in that color range no more than 20 foreground stars and background galaxies and no member star in other evolutionary phases can be expected, and (3) the completeness is much larger than 75% (indeed, it is almost 100%) and the effect of blending is negligible at the position of the tip in the WF cameras (Regions 0-4, see Section 4.2). The severe crowding and high degree of contamination from brighter

stars prevent instead a safe identification of the TRGB in the PC data.

5.1. TRGB detection

First of all, we have calibrated our data also into the Johnson-Cousins photometric system following the Holtzman et al. (1995b) prescriptions. Then we have applied the edge-detection algorithm based on the Sobel's filter to the LF of the upper RGB, as in SMF96. The measure has been performed separately for each camera and the results are presented in Fig.11. The left panels of Fig.11 report the I vs $V - I$ CMDs of the upper RGB for each WF camera (from top to bottom: WF2, WF3, and WF4, respectively). In these CMDs the RGB stands out very clearly and the tip discontinuity is evident. The right panels of Fig. 11 show the corresponding LFs (here presented as generalized histograms, see Ikuta & Arimoto 2000, and references therein) and the response of the edge-detection filter to these LFs. The TRGB is clearly and uniquely detected in each of the WFs as the highest peak in the Sobel Filter Response. The derived estimates are reported in the plots showing the Sobel Filter Response as a function of the I magnitude, the quoted errors being the HWHM of the peaks corresponding to the TRGB detections. The agreement between the three independent measures is excellent, and we adopt their mean as the final estimate, i.e. $I(TRGB) = 24.62 \pm 0.08$. Adopting $E(B-V) = 0.045$ from O'Connell et al. (1995) and $A_I = 2.0\,E(B-V)$, derived from Dean, Warren, & Cousins (1978), we finally obtain $I_0(TRGB) = 24.53 \pm 0.10$, including also a $\pm\,0.02$ uncertainty associated to the reddening estimate.

5.2. Distance modulus from I(TRGB)

A serious source of uncertainty for distance moduli estimated via the TRGB method resides in the calibration of the absolute magnitude $M_I(TRGB)$ as a function of metallicity (see Salaris & Cassisi 1998 for a detailed discussion). Bellazzini, Ferraro, & Pancino (2001, hereafter BFP01) recently provided a new empirical calibration of $M_I(TRGB)$ as a function of $[Fe/H]$, in the range $-2.3 \leq [Fe/H] \leq -0.2$. The new calibration is in agreement with previous ones (Da Costa & Armandroff 1990; Ferrarese et al. 2000) within the uncertainties, but has a much safer and robust observational basis (see BFP01 for details).

Thus we adopt their eq. 4, averaging over the whole $[Fe/H]$ range. In the "standard" technique (SMF96) the distance modulus and the mean metallicity of the population are simultaneously estimated by an iterative process. We prefer a more conservative approach, considering the metallicity as an unknown factor, therefore a mere source of uncertainty. The complete error budget of the final distance modulus is the following: $\pm\,0.1$ mag from the uncertainty in the dereddened $I_0(TRGB)$, $\pm\,0.06$ mag due to the lack of knowledge of the metallicity of the population, $\pm\,0.12$ mag from the uncertainty on the TRGB calibration (see BFP01), and $\pm\,0.2$ mag as a conservative assumption of the global uncertainty of the absolute photometric calibration (including uncertainties in zero

points, aperture corrections, short vs. long anomaly, etc.).

Considering all these possible sources of error, our final best estimate of the distance modulus of NGC 1705 is $(m-M)_0 = 28.54 \pm 0.26$, which corresponds to a distance $D = 5.1 \pm 0.6$ Mpc.

At this distance, $1''$ corresponds to 24.8 pc and the horizontal bar in the bottom right corner of Fig. 2 indicates the apparent length of 100 pc. The PC covers an area of $893 \times 893\,\mathrm{pc}^2$ and NIC2 an area of $472 \times 472\,\mathrm{pc}^2$.

6. Comparison with stellar evolution models

For an easier interpretation of the CMD in terms of stellar evolutionary phases, in Fig. 12 we have superimposed on the empirical optical CMD the Padua stellar evolution tracks with metallicity likely to be appropriate for NGC 1705 (Z=0.008, Z=0.004 or Z=0.0004, Fagotto et al. 1994a, b). The CMD refers to the 17842 stars of the whole WFPC2 field, most tightly selected on the basis of DAOPHOT parameters (i.e. with $\sigma_{DAO} \leq 0.1$ in both F555W and F814W, and the values of χ^2 and *sharpness* described in Section 2). The theoretical tracks have been transformed into the observational plane by adopting E(B–V) = 0.045 and $(\mathrm{m–M})_0 = 28.54$ (see previous section) and the tables for bolometric correction and temperature–color conversion in the HST VEGAMAG photometric system from Origlia & Leitherer (2000).

The plotted tracks are for masses in the range 0.9 – 30 $M_\odot$. Due to their long lifetimes (in these sets a 0.8 $M_\odot$ reaches the TRGB in 19 Gyr), at the distance of NGC 1705 lower-mass stars wouldn't have had time to reach visible phases within a Hubble time. For high- and intermediate-mass stars we have plotted all the evolutionary phases, while for low-mass stars (i.e. $\leq 1.7\ M_\odot$) we have drawn them only up to the TRGB, to avoid excessive confusion. The MS corresponds to the almost vertical lines at $-0.3 \leq m_{F555W} - m_{F814W} \leq -0.1$ and the turnoff is recognizable as a small blue hook. Of the later evolutionary phases, we can clearly distinguish the almost horizontal blue loops corresponding to core helium burning, the bright red sequences of the AGB of intermediate-mass stars and the fainter red sequences of the RGB of low-mass stars, terminating at the TRGB with approximately the same luminosity. The only observed feature which has not a theoretical counterpart is the almost horizontal tail extending redwards of $m_{F555W} - m_{F814W} = 2$ at m_{F814W} just fainter than 24. Given its position at the edge of the AGB and TRGB, we tend to ascribe it to thermally pulsing AGB stars, a poorly understood evolutionary phase whose models are not displayed in the adopted tracks.

Whatever the assumed metallicity, from the tracks overlap on the empirical CMD of the whole observed region, it turns out that the blue plume of NGC 1705 is populated by both intermediate- and high-mass stars on the MS and by massive stars at the blue edge of the core helium burning phases, the red plume is populated by RSGs and AGB stars, and the faint red clump with $1 \lesssim m_{F555W} - m_{F814W} \lesssim 2$ and $24.5 \lesssim m_{F814W} \lesssim 26.5$ is populated by RGB stars. It is also apparent that very few stars more massive than 30 $M_\odot$ are likely to be present in the resolved field of the

galaxy. The more massive objects present in significant numbers in the empirical CMD appear to be stars of 15–30 $M_\odot$. In fact the theoretical tracks corresponding to this mass range can account for several objects spanning in the CMD from blue to red colors and connecting the blue and the red plume with a sort of bright bridge. This suggests that an enhancement of the SF activity has probably occurred at the epoch corresponding to the lifetime of a 20 $M_\odot$, i.e. around 15 Myr ago.

Fig. 13 shows the analogous superposition of the same three sets of evolutionary tracks on the most tightly selected CMD derived from the NIC2 data and containing 829 stars. The strong differential effect due to the severe incompleteness affecting blue faint objects in these bands (see also Al01) results in the extreme paucity of blue plume stars already mentioned in Section 4. The red vertical *finger* is populated by RSGs and AGB stars, while the RGB is too faint to be reachable with these stars so restrictively selected; we do reach it if we relax the σ_{DAO} criterion (see Fig. 5) to $\sigma_{DAO} \leq 0.2$. In agreement with what we find for the optical CMD, stellar models with 15–30 $M_\odot$ fit quite well the bridge of brightest points connecting the blue and the red plume.

An accurate estimate of the oxygen abundance in NGC 1705 was given by Storchi-Bergmann et al. (1994), who derive $12 + \log(\mathrm{O/H}) = 8.36$ from HII regions. This implies that the youngest objects have a metallicity of about $Z = 0.004$. No direct information is available for older objects. The stellar metallicities (Z slightly higher or slightly lower than that of the LMC) quoted by MFDC and Sternberg (1998) are only indicative. Wide band photometry is certainly not the best way to infer metal abundances, but we can provide some hints. By simply comparing the color distributions of theoretical tracks and observed objects in the CMDs of both Fig. 12 and Fig. 13, it is apparent that the vast majority of the stars resolved in NGC 1705 are more metal-rich than $Z = 0.0004$, including the old stars on the RGB. In fact, even accounting for the large uncertainties in the photometric conversions from the theoretical to the observational plane and for the photometric errors of the data, this set of stellar models appears to be too blue to be reconcilable with the observed optical and NIR colors in all the red evolutionary phases. On the other hand, the $Z = 0.008$ models seem slightly too red, specially in the red CMD region. In this case, we cannot exclude that the effect is due to conversion errors, rather than to a real metallicity excess; however, we tend to exclude that metallicities higher than this could be appropriate for this galaxy.

7. Discussion and conclusions

We have acquired deep HST photometry of the nearby BCD NGC 1705 to resolve its stellar populations and derive information on its evolution. With the images in F555W, F814W, F110W, and F160W obtained with the use of WFPC2 and NICMOS, we are able to detect for the first time about 40,000 field objects and to sample both the young and the old resolved stellar populations. We have also detected several candidate star clusters (besides the SSC) and background galaxies (including a yet unclassified galaxy cluster). These composite objects will be described in a forthcoming paper (Monelli et al. in preparation), where also the F380W and F439W images will be

analyzed.

The excellent performance of HST allows us to measure also the fainter/older stars in the RGB phase and to clearly identify in the WFs the TRGB at $m_{F814W} \simeq 24.5$, a luminosity level more than 2 mag brighter than our most conservative limit, where both incompleteness and blend are not yet significant. Thanks to this result, we have derived from the TRGB I luminosity in the Johnson–Cousins photometric system a distance modulus $(m-M)_0 = 28.54 \pm 0.26$ (i.e. a distance of 5.1 $\pm$ 0.6 Mpc) in excellent agreement with the modulus (28.5 ± 0.7) of O'Connell et al. (1994) and consistent with MFDC's distance (4.7 Mpc).

NGC 1705 is considered a *post-starburst* galaxy, because even the SSC, where the SF activity has been more concentrated and recent, has stopped forming stars at least 5–6 Myr ago, as argued by Heckman & Leitherer from the lack of spectral features from O and Wolf–Rayet (WR) stars. Our data show that also outside the SSC there are only a few stars more massive than 30 $M_{\odot}$, and most of them seem to be connected to the brightest SSC, through the pearl necklace shown in Fig. 2. This paucity of very massive stars is in agreement with MFDC who identified only 5 candidate HII regions and one extended ionizing association (g+h in their nomenclature) with emission-line features indicating the presence of WR stars. We thus suggest that the most recent conspicuous SF activity in the field of NGC 1705 has occurred approximately 10–20 Myr ago.

NGC 1705 definitely contains a a significant population of stars several Gyr old. This does not imply, though, that the galaxy population is essentially old. By separating, with the help of the Padua stellar evolution tracks, the observed optical CMD in three different zones corresponding to different stellar masses, we find that in the PC field, which at our derived distance covers a region of about $893 \times 893\,\mathrm{pc}^2$, of the 9224 stars most tightly selected, 50% have masses ≥ 3 $M_{\odot}$ and, hence, age lower than 500 Myr, and $\sim$800 (9%) have masses ≥ 7 $M_{\odot}$, and are thus younger than 60 Myr.

From *bona fide* RGB stars, we can estimate also the fraction of the oldest objects. As apparent from Fig. 12, the color of the RGB depends strongly on the metallicity: if Z = 0.008, the blue edge of our resolved RGB stars is $m_{F555W} - m_{F814W} \simeq 1.4$, if Z = 0.004, it is around 1.2, and, if Z = 0.0004, it is around 1.0. If we consider as RGB stars all those with $m_{F814W} \geq 24.5$ and $m_{F555W} - m_{F814W}$ redder than these blue edges, we find that 3511, 2398 or 1227 (for Z = 0.008, 0.004, or 0.0004, respectively) over 9224 stars are older than 1 Gyr. In other words, thanks to the higher resolving power of the HST, we have been able to measure also in the inner $893 \times 893\,\mathrm{pc}^2$ the oldest population, which was too faint to be resolvable with ground-based observations.

The diagrams of Fig. 4 confirm the existence of an age gradient. We find that:

- the most massive stars (M $\lesssim$ 30 $M_{\odot}$), younger than 10–20 Myr, are all located within 100 pc from the galactic center and the most luminous SSC, most of them in Region 7 and a few in Region 6;
- intermediate-mass stars with ages up to 1 Gyr are visible only in Regions 6 and 5, i.e. within $\sim$500 pc from the center. Some of them are present also in Region 7, but the extreme

crowding and high background of this zone makes their detection highly improbable;

- beyond ~ 500 pc from the center, the galaxy is populated only by low mass stars on the RGB, i.e. with ages from a few Gyr to a Hubble time.

As mentioned in the Introduction, previous studies already pointed out that NGC 1705 has a composite population (Quillen et al. 1995), with an age gradient (MFDC) like the one here described. This is, however, the first evidence from direct analysis of the resolved stellar populations. The same kind of spatial segregation of the younger stars has been found also in other late-type dwarfs (e.g., NGC 1569, G98; I Zw 18, ATG; VII Zw 403, Schulte-Ladbeck et al. 1999a).

In summary, NGC 1705 is definitely not a starburst galaxy, since it does not appear to have had any conspicuous SF activity in the last few Myrs, neither in the field nor in the SSC. Our CMDs show that the last episode of significant SF in the field has occurred around 10–20 Myr ago, preceded by several other episodes or by a continuous activity. To understand whether or not any of these episodes can be considered as a real burst (i.e. short and intense SF activity), and how long the quiescent phases (if any) have lasted, one must perform a more sophisticated analysis. We are working on this analysis using the method of synthetic CMDs described by Tosi et al. (1991) and G98, and the results will be presented in a forthcoming paper (Annibali et al. in preparation).

The impressive morphology of the H_α images of the galaxy, dominated by loops and arcs apparently centered on the brightest SSC, and the corresponding kinematics have been studied by MFDC. They interpreted the loops and arcs as hot expanding bubbles energized by supernova ejecta and stellar winds from its nucleus, with estimated expansion timescale of $\sim$9 Myr. Recent FUSE observations of NGC 1705 (Heckman et al. 2001) also show that the superbubbles will most probably blow out of the galaxy and remove a significant fraction of its metals. Sahu & Blades (1997) agreed with this scenario of conspicuous galactic wind triggered by supernova explosions, on the basis of HST UV spectra. Their data confirmed the 540 km s^{-1} velocity of the supershell and showed the overabundance in the galaxy gas of elements produced by massive stars. X-ray observations (Hensler et al. 1998) supported the same picture, and the discovery of an extremely soft component in the X-ray emission led these authors to suggest that the SSC is not located at the galactic center, a possibility already considered by Heckman & Leitherer (1997) and confirmed by our images and by the isophotal contours shown in Fig. 1. It would be interesting to check whether the pearl necklace of bright young stars and the asymmetric distribution of the candidate star clusters displayed in Fig. 2 are physically related to the SSC impact on the surrounding environment.

Quantitative information on the star formation history of NGC 1705 will be useful also to assess the effect of galactic winds on the chemical enrichment of its ISM. This galaxy has clearly formed stars over several Gyrs, most of its old stars have a fairly high metallicity of $Z = 0.004$, and yet it is characterized by strong winds currently removing heavy elements from its ISM. Was the early metallicity high because of a very strong initial SF ? Is the current wind event the first one occurring over the galaxy lifetime ? If this is the case, why have not early SF episodes been able

to trigger the winds (especially if the earliest activity was strong) ? Or does it mean that winds do not significantly affect the galaxy metallicity (for instance, because they involve too small amounts of gas, or because after some time the metals fall back on the galaxy) ? To try to answer these questions, quantitative estimates of the SF rate and of the IMF are necessary. Our forthcoming results from the synthetic CMD method will provide such information, since we will derive the epoch, the duration and the intensity of each major SF episode, and we will infer indications on the most likely IMF.

Very preliminary results (Annibali et al. 2001) indicate that indeed NGC 1705 has been forming stars since 10–15 Gyr, with different rates at different epochs, but without evidence of strong bursts or really quiescent intervals. They also suggest that the IMF of the young stellar populations is flatter than normal (with a slope $\alpha \simeq 1.5$ in the usual approximation $dN/dm \propto m^{-\alpha}$, where Salpeter's slope is 2.35), therefore implying a fraction of massive stars higher than normal. This unusual IMF, even if relative to the field stars and not to the SSC stellar population, is in agreement with one of the two Sternberg's (1998) arguments (the second one being a truncated IMF at a lower mass limit between 1 and 3 $M_{\odot}$) to explain the SSC overluminosity, which at our derived distance of 5.1 Mpc is indeed confirmed. More accurate and extensive tests in the various Regions, as well as the photometric reduction and analysis of the F380W and F439W data, are however necessary to reach firmer conclusions and are currently being performed (Annibali et al. in preparation; Monelli et al. in preparation).

We thank Luis E. Bergeron, Stefano Casertano, Mark Dickinson, Luciana Federici, and Matteo Monelli for help and suggestions to overcome the data reduction problems. Daniela Calzetti, Mark Clampin, Jay Gallagher, Antonella Nota, Livia Origlia, and Lucia Pozzetti are warmly thanked for useful information and discussions. This work has been partly supported by the Italian ASI, through grants ARS-96-70 and ARS-99-44, and by the Italian MURST, through Cofin2000. Support for this work was also provided by NASA through grant number GO-07881.01-96A from the Space Telescope Science Institute. Funding for A.A. has also been provided through an Italian CNAA fellowship. E.S. thanks the STScI for the hospitality during a one month visit, partially funded by a fellowship from the University of Bologna.

REFERENCES

Aloisi, A., Clampin, M., Diolaiti, E., Greggio, L., Leitherer, C., Nota, A., Origlia, L., Parmeggiani, G., & Tosi, M., 2001, AJ, 121, 1425 (Al01)

Aloisi, A., Tosi, M., & Greggio, L. 1999, AJ, 118, 302 (ATG)

Annibali, F., Aloisi, A., Greggio, L., Leitherer, C., & Tosi, M., 2001, in Dwarf Galaxies and their Environment, K.S. de Boer, R.J. Dettmar, U. Klein eds (Shaker Verlag, De), in press

Babul, A., & Ferguson, H.C. 1996, ApJ, 458, 100

Baggett, S., Casertano, S., Gonzaga, S., & Ritchie, C. 1997, ISR WFPC2 97-10

Baggett, S., & Gonzaga, S. 1998, ISR WFPC2 98-03

Bellazzini, M, Ferraro, F.R., & Pancino, E., 2001, ApJ, in press, astro-ph/0104114

Bessell, M.S., Castelli, F., & Pletz, B. 1998, A&A , 337, 321

Biretta, J.A., et al. 2000, WFPC2 Instrument Handbook, Version 5.0 (Baltimore: STScI)

Casertano, S., & Mutchler, M. 1998, ISR WFPC2 98-02

Da Costa, G.S., Armandroff, T.E., 1990, AJ, 100, 162

Dean, J.F., Warren, P.R., & Cousins, A.W.J., 1978, MNRAS, 183, 569

Dickinson, M., 1999, "NICMOS Data Handbook", Version 4.0 (Baltimore, STScI)

Fagotto, F., Bressan, A., Bertelli, G., & Chiosi, C. 1994, A&AS, 104, 365

Fagotto, F., Bressan, A., Bertelli, G., & Chiosi, C. 1994, A&AS, 105, 29

Ferrarese, L., et al., 2000, ApJS, 128, 431

Fruchter, A.S., & Hook, R.N. 1998, PASP, submitted, astro-ph/9808087

Greggio, L., Tosi, M., Clampin, M., De Marchi, G., Leitherer, C., Nota, A., & Sirianni, M. 1998, ApJ, 504, 725 (G98)

Heckman, T.M., Lehnert, M.D., & Armus, L. 1993, in The Evolution of Galaxies and their Environments, S.M. Shull & H.Thronson eds (KLuwer, Dordrecht), 455

Heckman, T.M., & Leitherer, C. 1997, AJ, 114, 69

Heckman, T.M., Sembach, K.R., Meurer, G.R., Strickland, D.K., Martin, C.L., Calzetti, D., & Leitherer, C., 2001, ApJ, in press, astro-ph/0102283

Hensler, G., Dickow, R., Junkes, N., & Gallagher, J.S. 1998, ApJ, 502, L17

Ho, L.C., & Filippenko, A.V. 1996, ApJ, 466, L83

Holtzman, J.A., Burrows, C., Casertano, S., Hester, J., Trauger, J., Watson, A., & Worthey, G. 1995a, PASP, 107, 1065

Holtzman, J.A., et al. 1995b, PASP, 107, 156

Hunter, D.A., & Thronson, H.A. 1995, ApJ, 452, 238

Ikuta, C., Arimoto, N., 2000, A&A, 358, 535

Izotov, Y.I., & Thuan, T.X. 1999, ApJ, 511, 639

Izotov, Y.I., Thuan, T.X., & Lipovetsky, V.A. 1997, ApJS, 108, 1

Larsen, T.I., Sommer-Larsen, J., Pagel, B.E.J. 2000, astro-ph/0005249

Lee, M.G., Freedman, W.L., Madore, B.F., 1993, ApJ, 417, 533

Lilly, S.J., Tresse, L., Hammer, F., Crampton, D., Le Fevre, O. 1995, ApJ, 455, 108

Madore, B.F., Freedman, W.L., 1995, AJ, 109, 1645 (MF95)

Madore, B.F., Freedman, W.L., 1998, in Stellar Astrophysics for the Local Group, VII Canary Islands Winter School of Astrophysics, A. Aparicio, A. Herrero and F. Sanchez Eds., Cambridge: Cambridge University Press, p. 305

Marconi, G., Matteucci, F., & Tosi, M. 1994, MNRAS, 270, 35

Matteucci, F., & Tosi, M. 1985, MNRAS, 217, 391

Melnick, J., Moles, M., & Terlevich, R. 1985, A&A, 149, L24

Meurer, G.R, Freeman, K.C., Dopita, M.A., Cacciari, C. 1992, AJ, 103, 60 (MFDC)

Meurer, G.R., Staveley-Smith, L., & Killen, N.E.B. 1998, MNRAS, 300, 1091

O'Connell, R.W., Gallagher, J.S., & Hunter, D.A. 1994, ApJ, 433, 65

Origlia, L. & Leitherer, C. 2000, AJ, 119, 2018

Ostlin, G. 2000, ApJ, 535, L99

Peimbert, M., Peimbert, A., & Ruiz, M.T. 2000, ApJ, 541, 688

Pilyugin, L.S. 1993, A&A, 277, 42

Piotto, G. & Zoccali, M., 1999, A&A , 345, 485

Pozzetti, L., Madau, P., Zamorani, G., Ferguson, H., Bruzual A., G. 1998, MNRAS, 298, 1133

Sahu, M.S., & Blades, J.C. 1997, ApJ, 484, 125

Sakai, S., Madore, B.F., Freedman, W.L., 1996, ApJ, 461, 713 (SMF96)

Salaris, M., & Cassisi, S. 1997, MNRAS, 289, 406

Salaris, M., & Cassisi, S. 1998, MNRAS, 298, 166 (SC98)

Schulte-Ladbeck, R.E., Hopp, U., Crone, M.M., Greggio, L. 1999a, ApJ, 525, 709

Schulte-Ladbeck, R.E., Hopp, U., Greggio, L., Crone, M.M., 1999b, AJ, 118, 2705

Sternberg, 1998, ApJ, 506, 721

Storchi-Bergmann, T., Calzetti, D. & Kinney, A. 1994, ApJ429, 572

Tosi, M., Greggio, L., Marconi, G., & Focardi, P. 1991, AJ, 102, 951

Whitmore, B., Heyer, I., & Casertano, S. 1999, PASP, 111, 1559

Fig. 1.— Mosaic of WFPC2 images of NGC 1705 in the F814W filter. North is up and the axes of the equatorial coordinate system are indicated. The field of view of the PC is $36'' \times 36''$, while that of each WF is $80'' \times 80''$. Isophotal contour levels are superimposed on the image (see text for details).

Fig. 2.— Right hand panel: NIC2 image of NGC 1705 in the F110W filter. Left hand panel: enlargement of a portion of the PC image of Fig. 1, with superimposed the box of the NIC2 field and the inner isophotal contours. Open circles identify candidate star clusters (see text). The bar in the bottom right corner gives the linear scale of the image at an assumed distance of 5.1 Mpc.

Fig. 3.— DAOPHOT photometric errors σ_{DAO} vs. calibrated magnitude in all filters: for optical filters the PC data have been plotted separately from the WF ones because of the different S/N.

Fig. 4.— CMDs of the stars measured in WFPC2 fields and selected with the criteria described in the text. The stars have been divided into six groups on the basis of the contour levels of Fig. 1. Regions 1, 2 and 3, 4 are grouped together because of their similar stellar populations and crowding conditions. The number of stars plotted in each box is labelled in the bottom right corner. The average size of the photometric errors, as derived from the artificial stars experiments, are indicated. The color error is evaluated at $m_{F555W} - m_{F814W}$=1.

Fig. 5.— CMDs of the stars measured in the NIC2 field. The top panels show m_{F160W} vs $m_{F110W} - m_{F160W}$ for all the objects selected in the two bands with the criteria described in the text. These have been divided into three groups on the basis of the contour levels of Fig. 1. The number of the stars plotted in each box is given in the bottom right corner. The average size of the photometric errors, as derived from the artificial stars experiments, are indicated. The color error is evaluated at $m_{F110W} - m_{F160W}$=1. The lower panels show m_{F160W} vs $m_{F555W} - m_{F160W}$ for the objects identified in all the four bands. The color error is evaluated at $m_{F555W} - m_{F160W}$ =2.

Fig. 6.— Diagrams of magnitude differences (input–output) vs input magnitude from the artificial star experiments in the F555W filter. From the outer to the innermost Region, the plotted stars are 93260, 18638, 23581, 17477, 3132 and 108, respectively. The standard deviations in 1 mag bins around m_{F555W} = 23, 25, 27 are indicated for each Region. The lines superimposed on the diagrams represent the local mean Δm and the $\pm$ 1 standard deviations.

Fig. 7.— Same as Fig. 6 for the F814W frame. The number of plotted stars is 86770, 16722, 22116, 18912, 5020, 373. The standard deviations around m_{F814W} =23, 25 and 27 are also given.

Fig. 8.— Same as Fig. 6 for the F110W (left panels) and F160W frames (right panels). The stars plotted for the F110W filter are 73601, 45388, 3500 from the bottom to the top panel, and their standard deviations are computed at m_{F110W} = 20, 22, 24. The stars in the F160W filter are 47745, 31815, 2638 and the standard deviations are computed at m_{F160W} =19, 21, 23.

Fig. 9.— Completeness levels superimposed on the CMDs of Fig.4 for the six WFPC2 Regions.

The levels are derived combining the completeness factor in the m_{F555W} band with that of the m_{F814W} band (see text). From top to bottom of each box the plotted lines correspond to completeness factors $CF = 0.95$ (thick line), $CF = 0.75$ (thin line), $CF = 0.50$ (thick line), and $CF = 0.25$ (thin line). An evenly spaced grid of blending vectors is also superimposed to the CMDs (thin lines with black dots) . The amplitude of these vectors is the average Δm described in the text, the dots indicate the direction of the vectors. The effect of such vectors become appreciable only for $m_{F814W} \geq 24$ in the regions 5 and 6, and $m_{F814W} \geq 26$ for regions 0-4 and only at extreme colors.

Fig. 10.— Same as Fig. 9 but for the CMDs of Fig.5.

Fig. 11.— Detection of the TRGB. Left panels: $(I, V-I)$ CMDs of the upper RGB for the three WF cameras. Right panels: the corresponding Luminosity Functions, shown as generalized histograms, coupled with the response of the Sobel Filter to the LFs. The peaks in the Sobel Filter response correspond to the position of the TRGB.

Fig. 12.— Optical CMDs of the 17842 stars selected in the WFPC2 fields with superimposed the Padua stellar evolutionary tracks (Fagotto et al. 1994a, b). The tracks in the top panel have metallicity Z=0.008, those in the middle one have Z=0.004 and those in the bottom panel have Z=0.0004. Only the following stellar masses are shown: from left to right, 30, 15, 9, 7, 5, 4, 3, 2, 1.8, 1.6, 1.4, 1.2, 1.0, 0.9 $M_{\odot}$. The corresponding lifetimes are (they slightly differ from one metallicity to the other) 7, 15, 35, 56, 110, 180, 370, 1120, 1300, 1630, 2520, 4260, 8410, and 12500 Myr, respectively.

Fig. 13.— Same as Fig.12, but for the NIR CMD of the 829 stars selected in the NIC2 field.

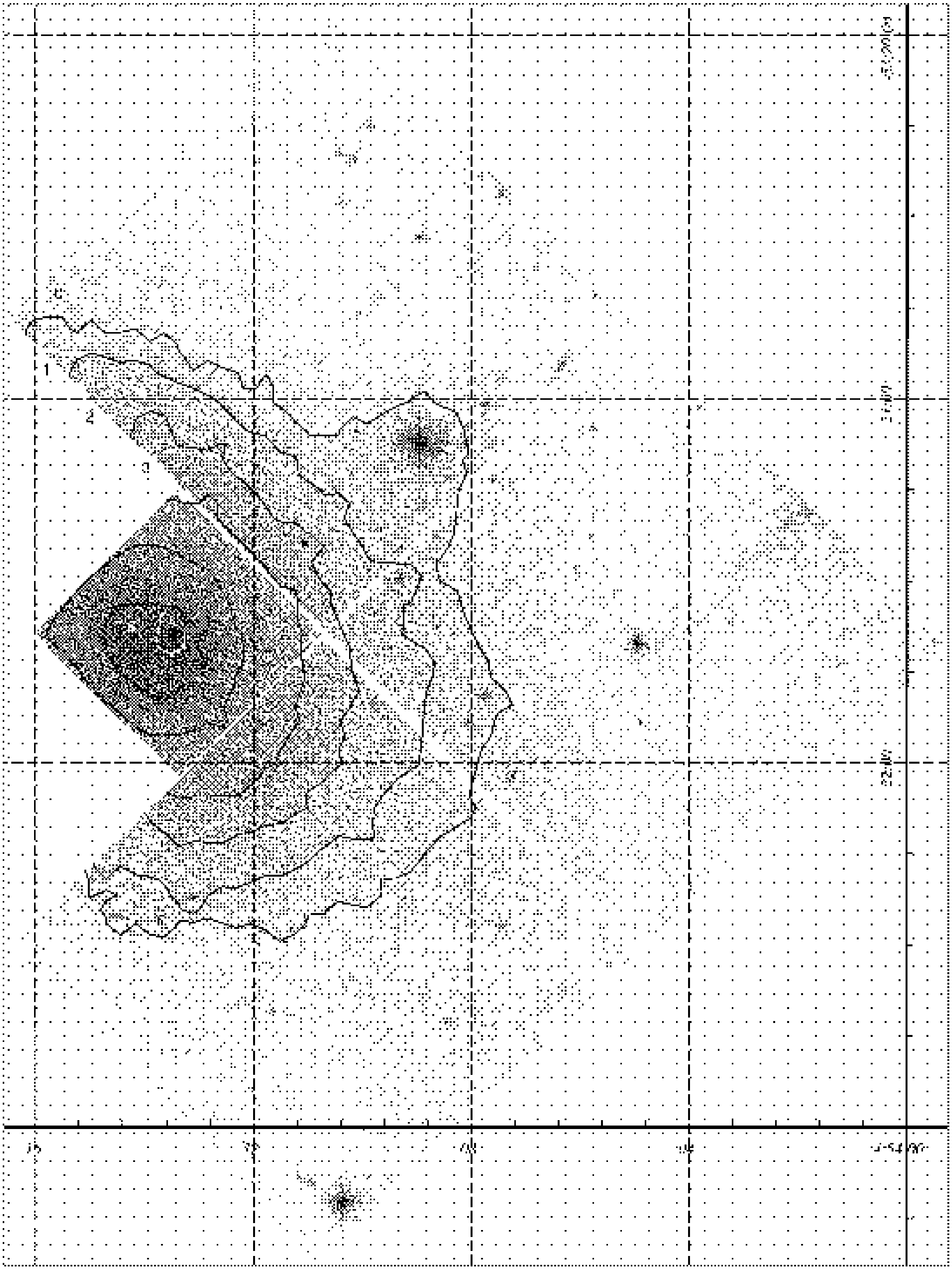

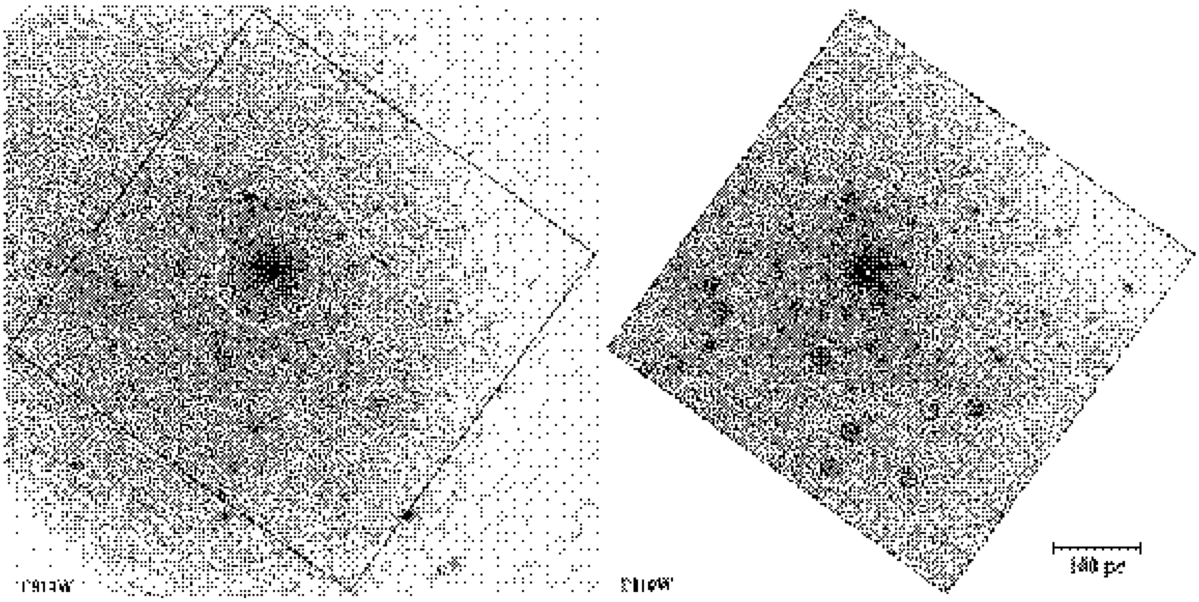

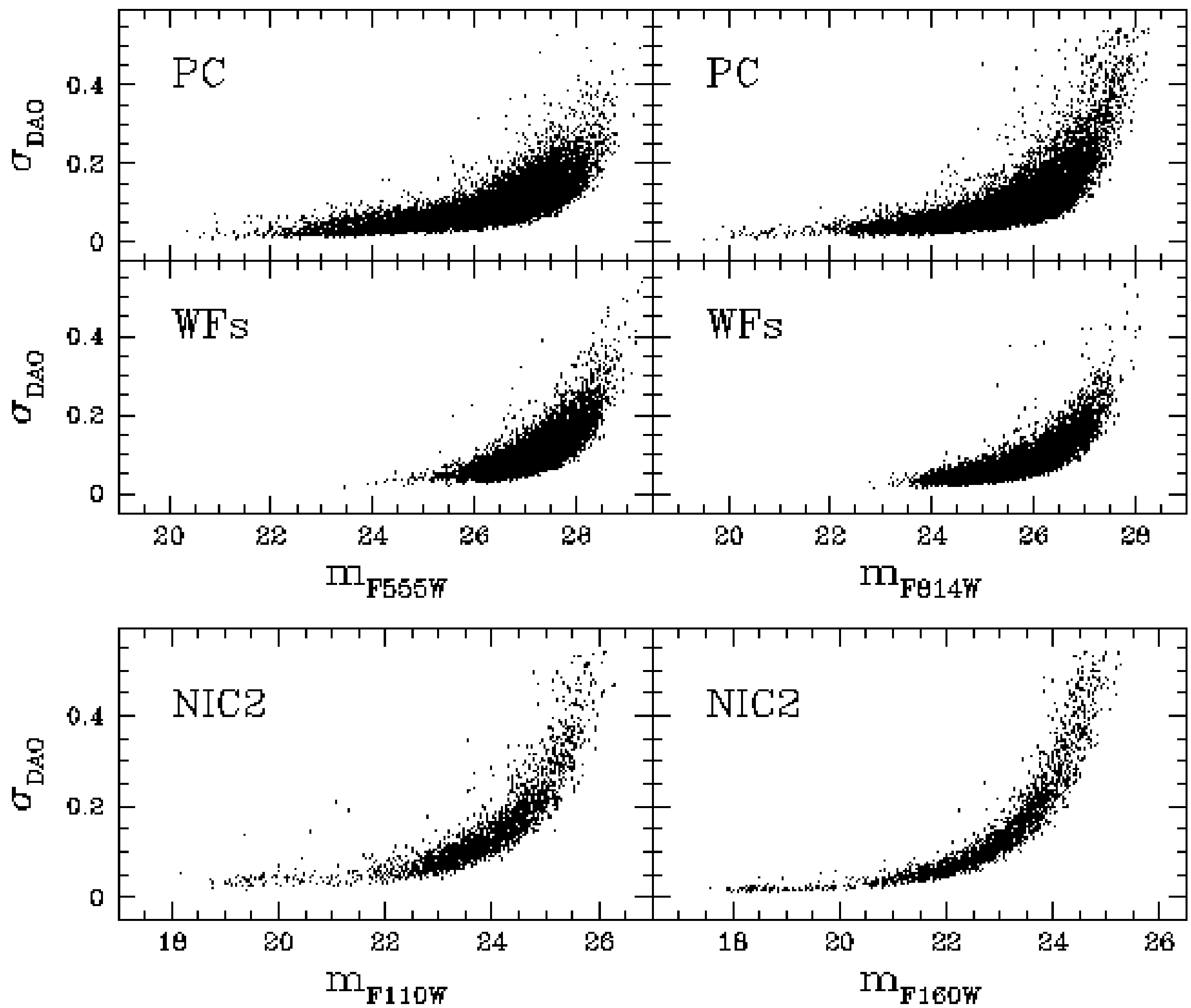
PC
PC
WFs
WFs
NIC2
NIC2
σ_{DAO}
0
0.2
0.4
20
22
24
26
28
18
m_{F555W}
m_{F814W}
m_{F110W}
m_{F160W}

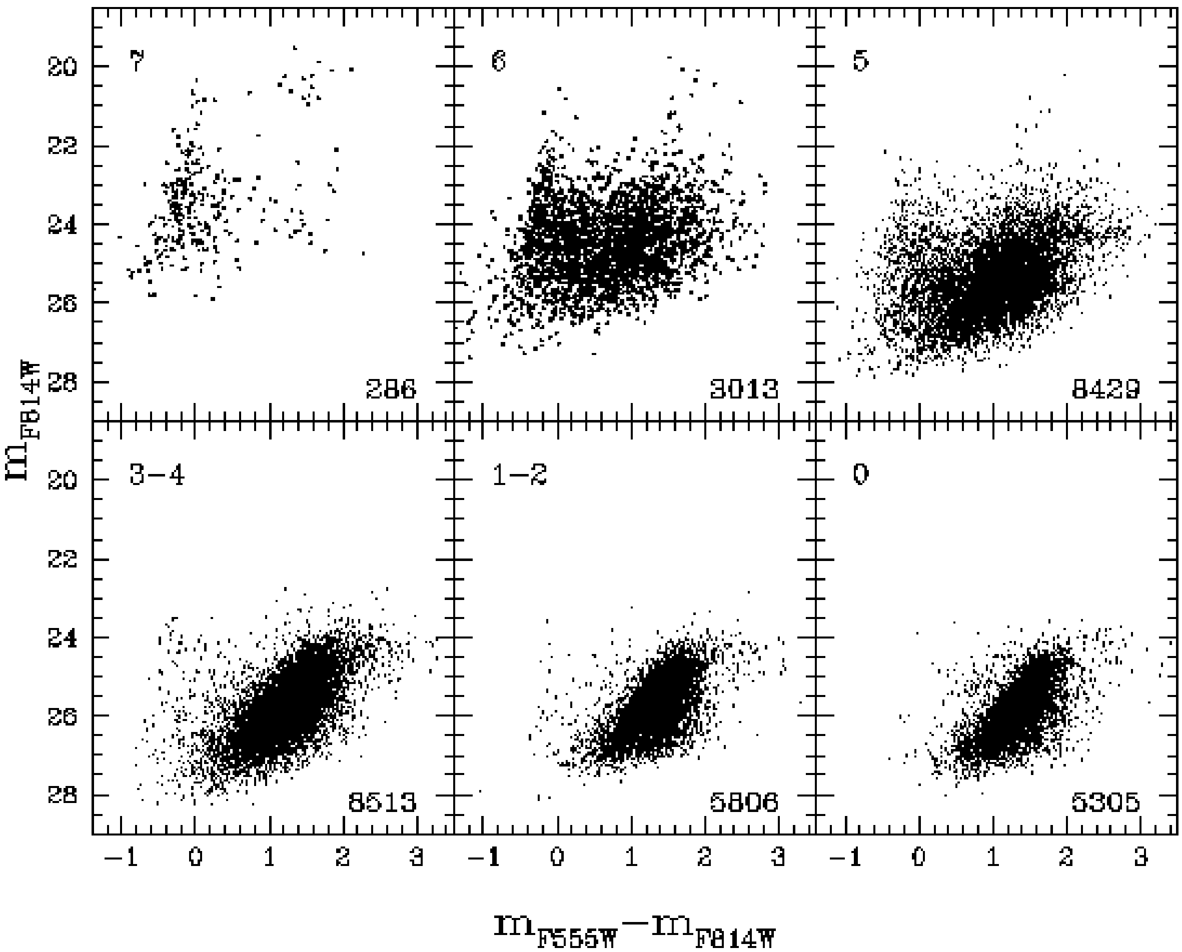
7
286
6
3013
5
8429
3-4
8513
1-2
5806
0
5305
20
22
24
26
28
−1
0
1
2
3
m_{F814W}
$m_{F555W}-m_{F814W}$

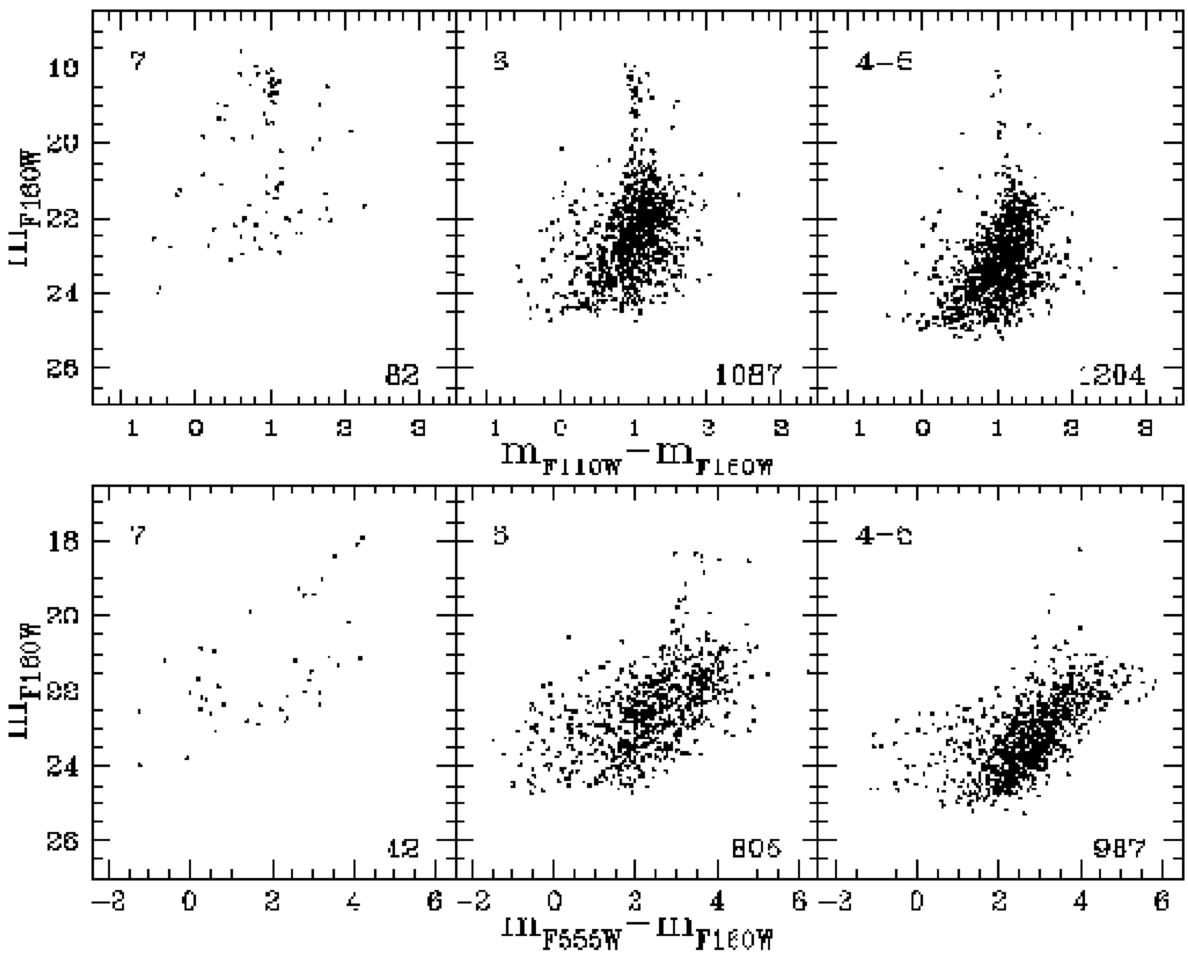
7
3
4–5
82
1087
1204
$m_{F110W}-m_{F160W}$
m_{F160W}
7
3
4–5
42
805
987
$m_{F555W}-m_{F160W}$
m_{F160W}

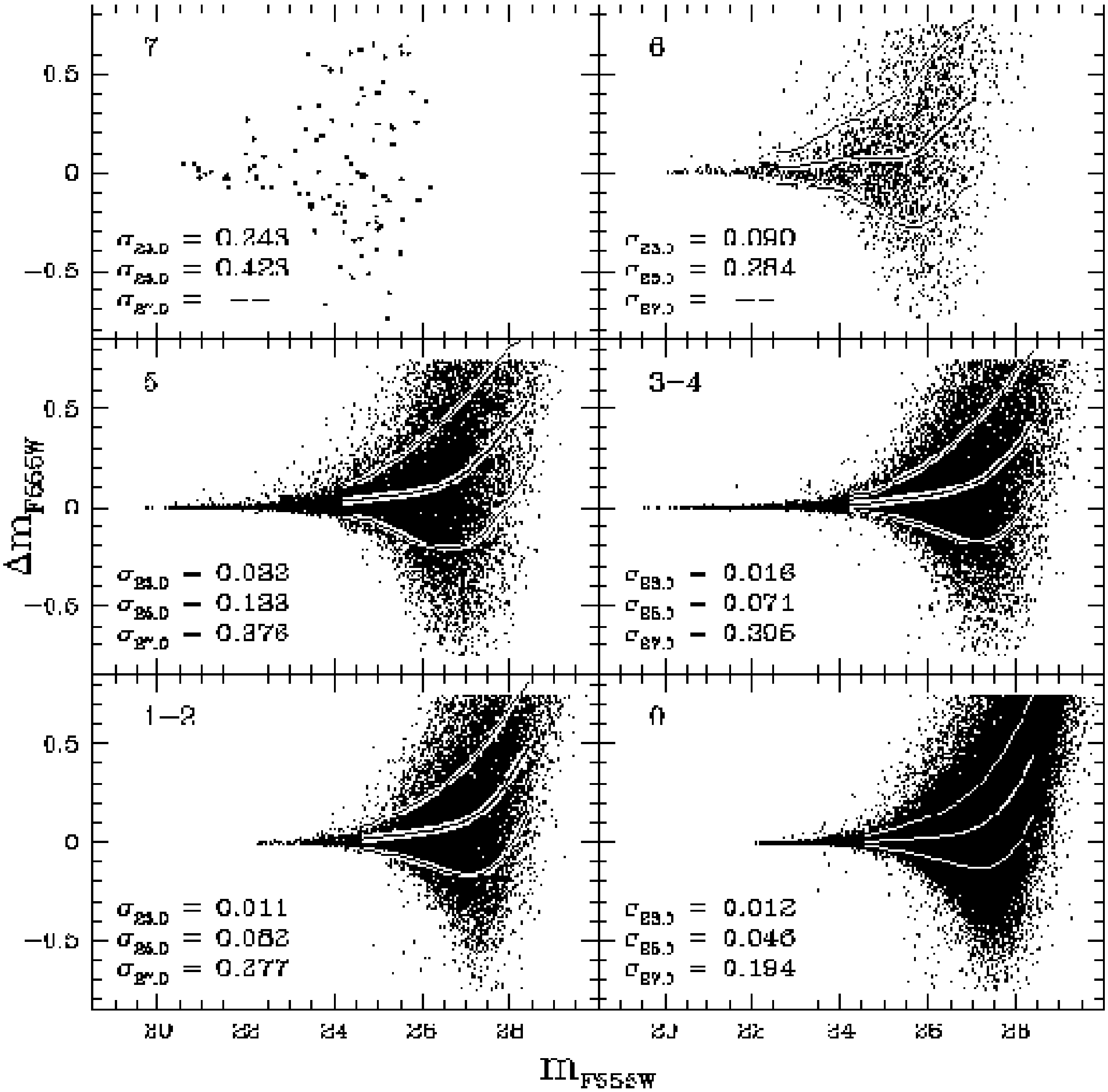
7
= 0.248
= 0.428
= ––
6
= 0.090
= 0.284
= ––
5
= 0.032
= 0.133
= 0.376
3–4
= 0.016
= 0.071
= 0.306
1–2
= 0.011
= 0.062
= 0.277
0
= 0.012
= 0.046
= 0.194
0.5
0
−0.5
20
22
24
26
28
Δm_{F555W}
m_{F555W}

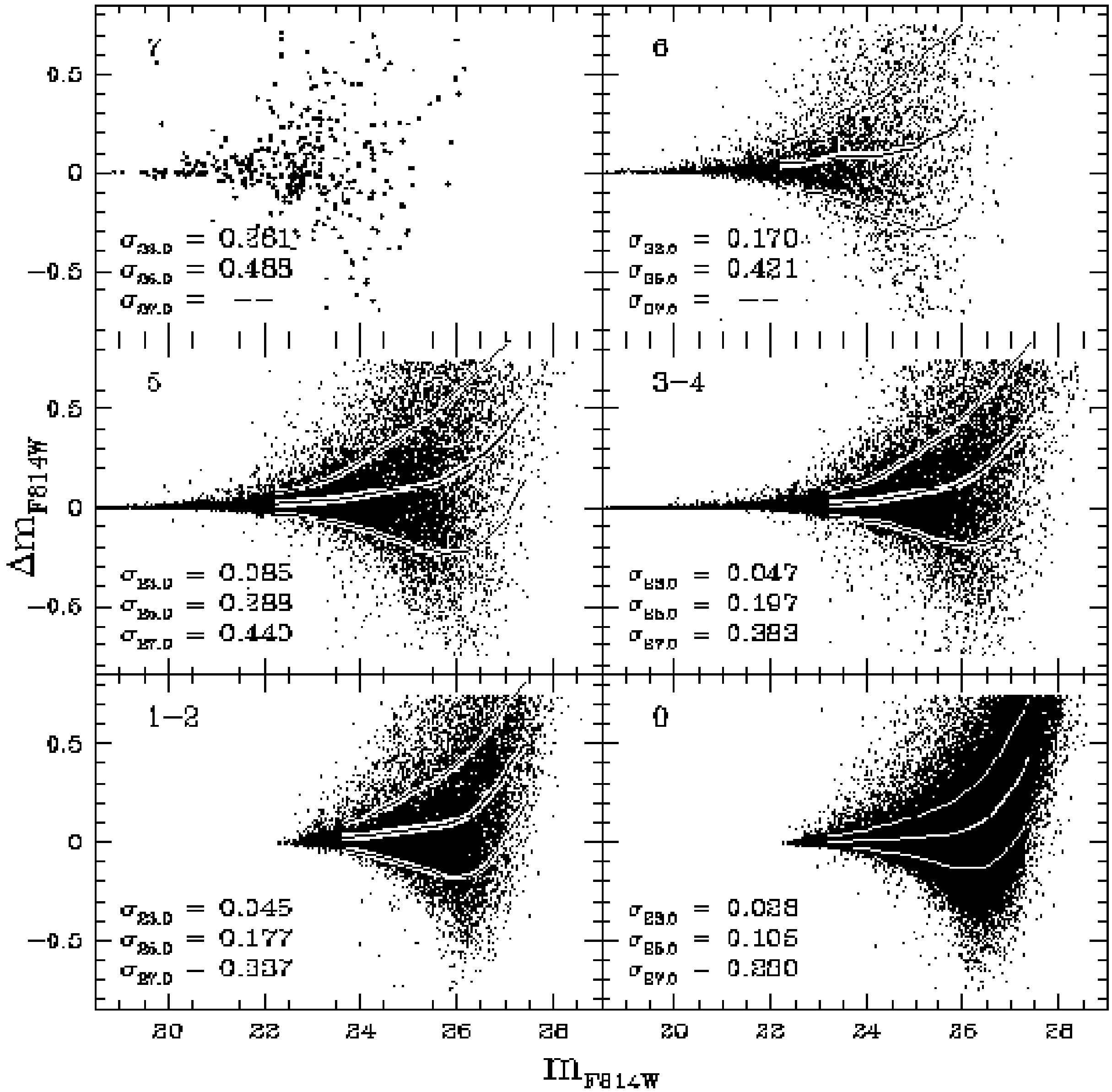
7
6
5
3−4
1−2
0
0.5
0
−0.5
20
22
24
26
28
Δm_{F814W}
m_{F814W}

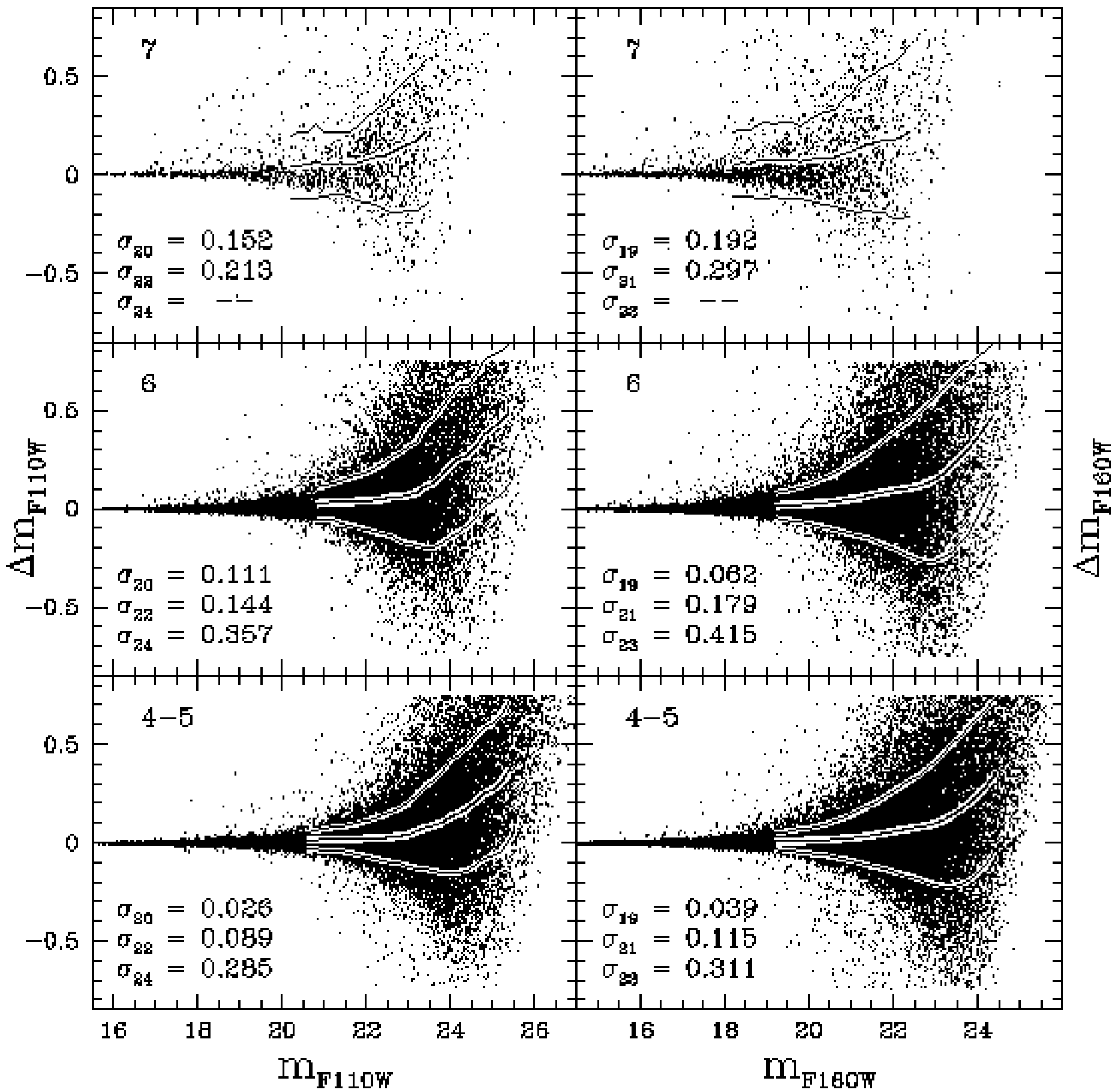
7
0.5
0
−0.5
σ20 = 0.152
σ22 = 0.213
σ24 = – –
7
σ19 = 0.192
σ21 = 0.297
σ23 = – –
6
Δm F110W
σ20 = 0.111
σ22 = 0.144
σ24 = 0.357
6
Δm F160W
σ19 = 0.062
σ21 = 0.179
σ23 = 0.415
4–5
σ20 = 0.026
σ22 = 0.089
σ24 = 0.285
4–5
σ19 = 0.039
σ21 = 0.115
σ23 = 0.311
16
18
20
22
24
26
m F110W
16
18
20
22
24
m F160W

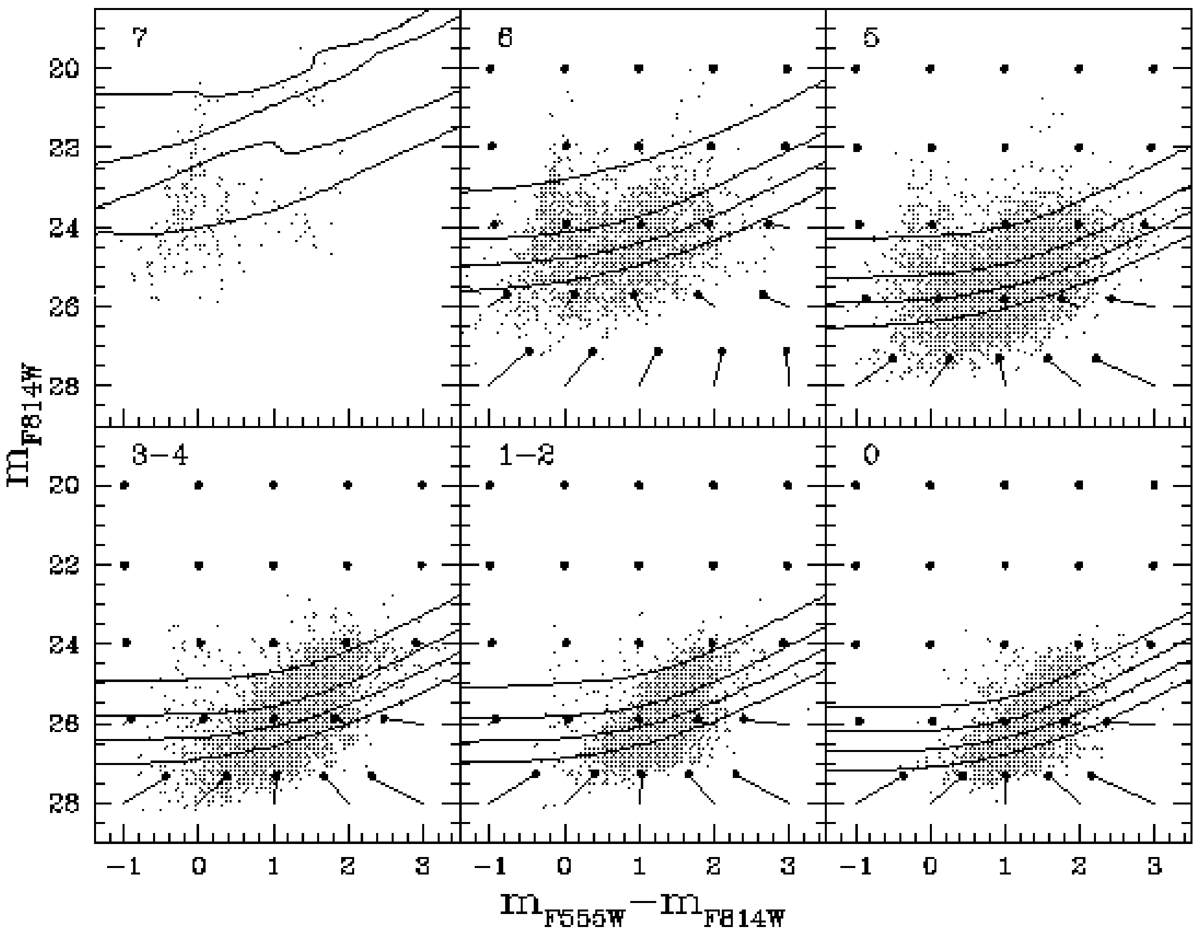
7
6
5
3−4
1−2
0
20
22
24
26
28
−1
0
1
2
3
m_{F814W}
$m_{F555W}-m_{F814W}$

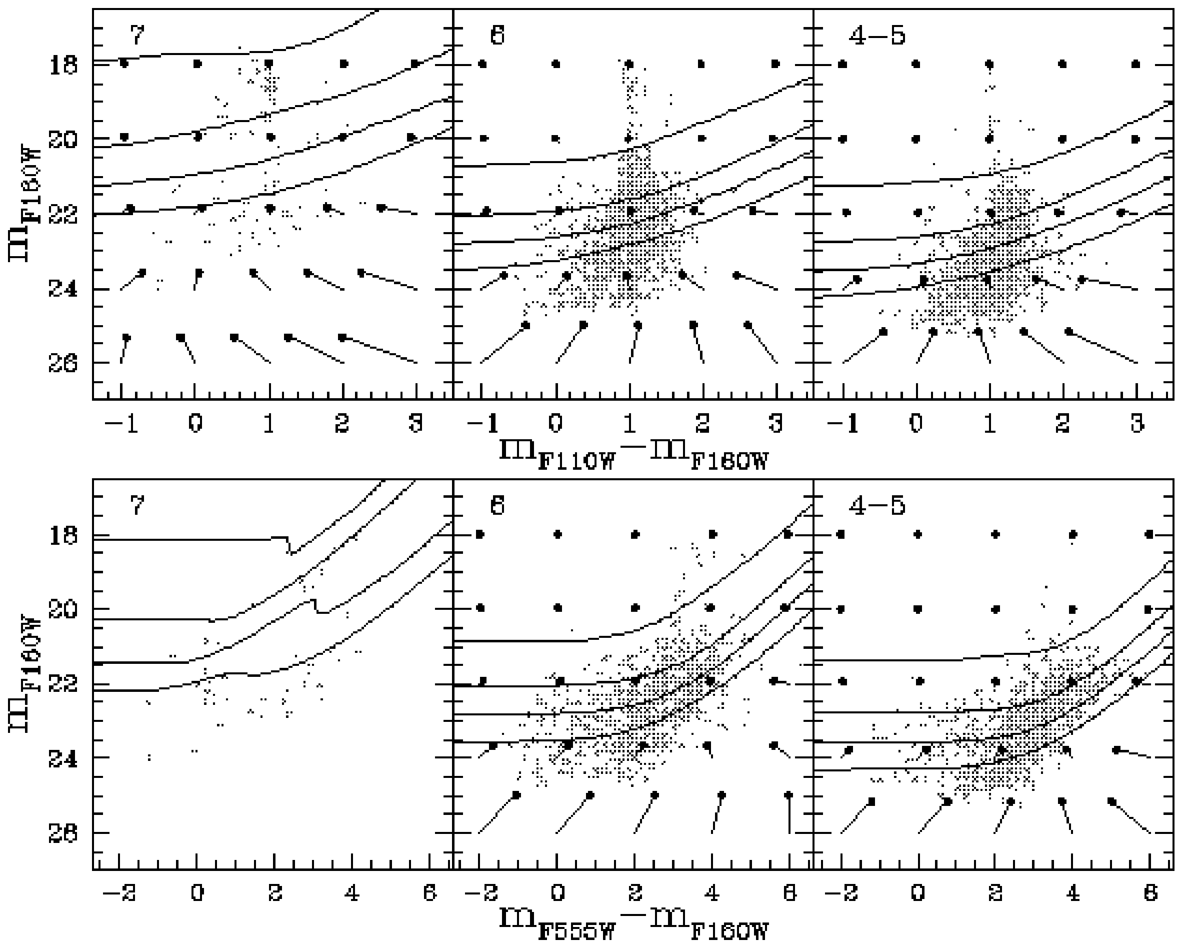
7
6
4−5
m_{F160W}
$m_{F110W}-m_{F160W}$
$m_{F555W}-m_{F160W}$

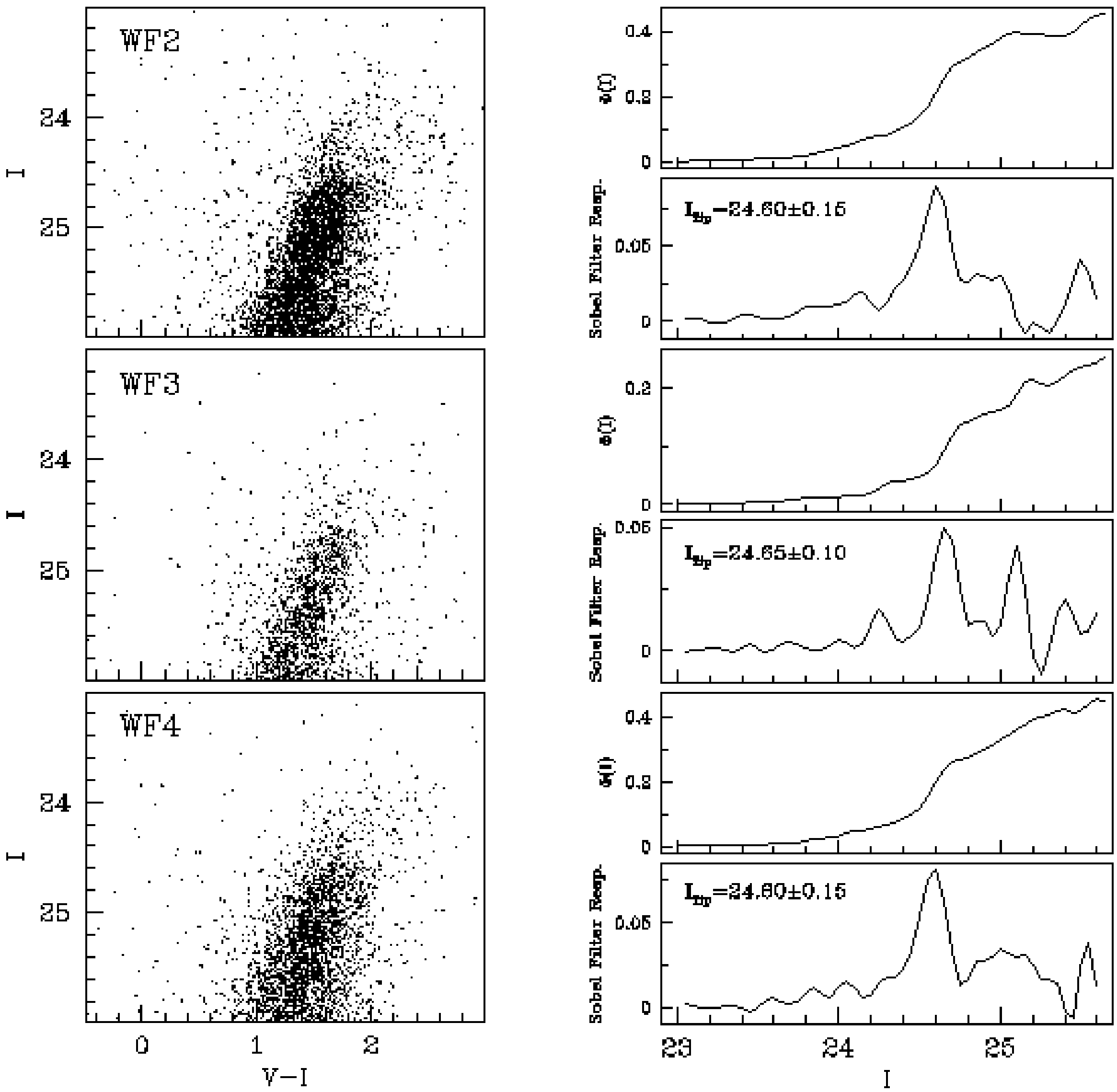

WF2
WF3
WF4
I
24
25
0
1
2
V−I
Φ(I)
0
0.2
0.4
Sobel Filter Resp.
0
0.05
I_{TRGB}=24.60±0.15
I_{TRGB}=24.65±0.10
I_{TRGB}=24.60±0.15
23
24
25
I

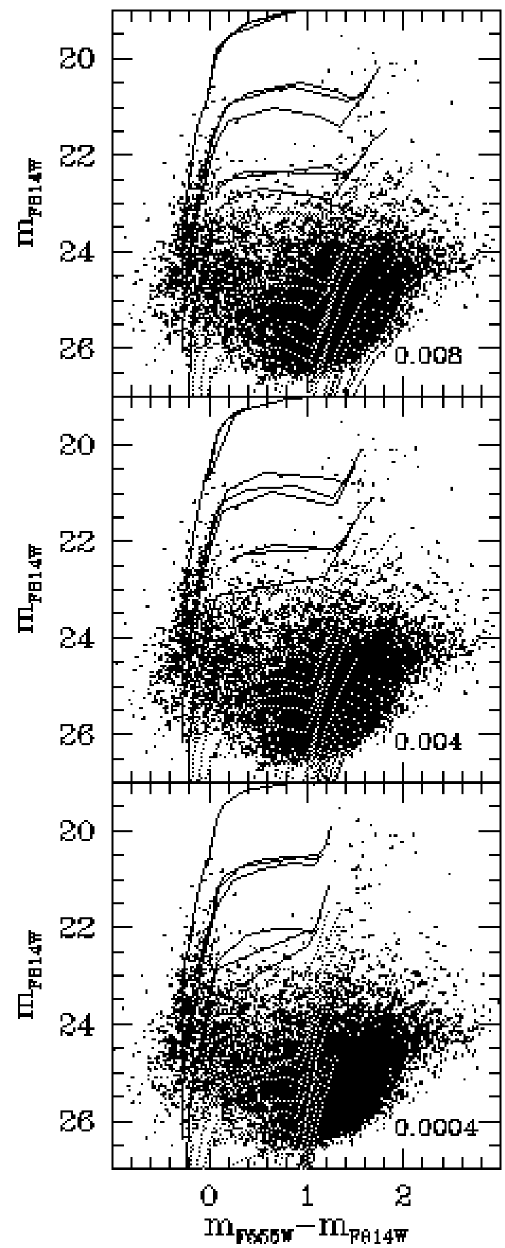
20
22
24
26
m_{F814W}
0.008
0.004
0.0004
0
1
2
$m_{F555W}-m_{F814W}$

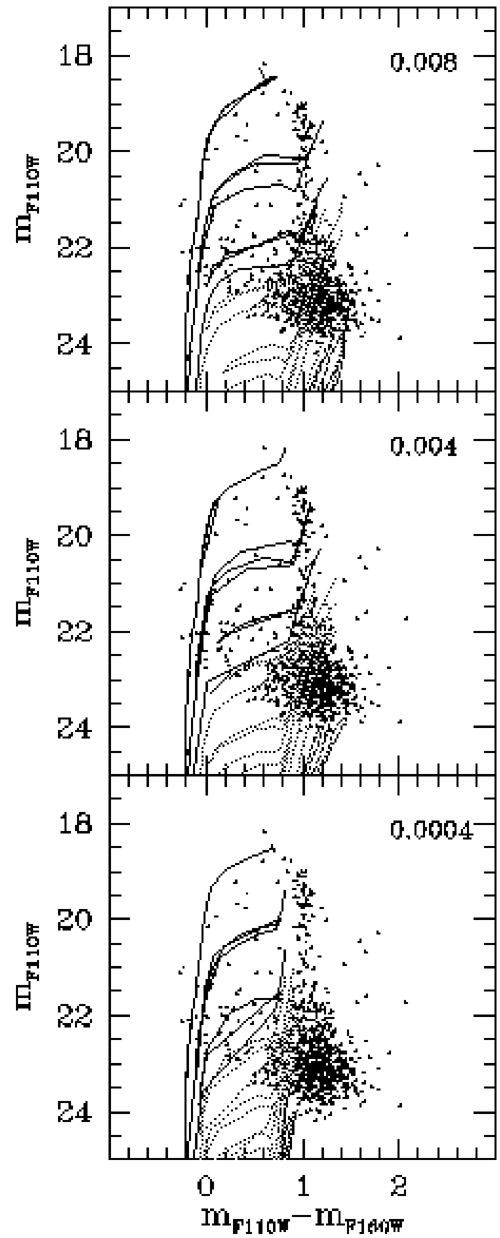
18
20
22
24
m_{F110W}
0.008
0.004
0.0004
0
1
2
$m_{F110W}-m_{F160W}$